The Effect of Rainfall on the Surface Layer during a Westerly Wind Burst in the Western Equatorial Pacific

H. W. WIJESEKERA, C. A. PAULSON, AND A. HUYER

College of Oceanic and Atmospheric Sciences, Oregon State University, Corvallis, Oregon

(Manuscript received 31 October 1997, in final form 12 May 1998)

ABSTRACT

Measurements of a fresh surface anomaly (fresh lens) produced by rainfall during a westerly wind burst have been analyzed. The measurements were made in December 1992 as part of the Coupled Ocean–Atmosphere Response Experiment in the western equatorial Pacific (2°S, 156°E). Measurements included radar estimates of rainfall, upper-ocean temperature (T), salinity (S), horizontal velocity, and microstructure. In situ observations of the fresh lens were made 5 to 7 hours after its formation. In the 5 hours after formation, the lens deepened to a depth of 40 m as indicated by its salinity anomaly. Salinity and temperature were highly correlated within the lens, consistent with its initial formation by cold rainfall. The T–S relation exhibited curvature, which can be explained by surface cooling and upper-ocean mixing subsequent to formation of the lens. The lens exhibited a horizontal velocity anomaly in the direction of wind, which extended down to a depth of 40 m. The horizontal velocity anomaly is consistent with momentum being trapped near the surface due to rain-induced stratification. Vertical velocity, estimated from the divergence of zonal velocity, showed downwelling at the leading edge of the lens and upwelling at the trailing edge. The magnitude of vertical velocity at a depth of 20 m is 20 m day^{-1}. Richardson numbers within the lens were low (0.25 to 0.5), suggesting that turbulent mixing was governed by critical-Ri instability. Wavenumber spectra of T and S in the upper 20 m exhibit a $-5/3$ range, which extends to wavenumbers below the range of local isotropy. Spectral levels were used to estimate turbulent dissipation rates of T and S, which were in turn used to estimate turbulent fluxes of heat and salt. Turbulent fluxes were also estimated from microstructure observations between depths of 10 and 60 m. Fluxes within the fresh lens were nearly uniform from 2 m to 35 m depth, then decreased to near zero at 45 m. The lifetime of fresh lenses during westerly wind bursts appears to be less than one day.

1. Introduction

The warmest and among the freshest open water in the World Ocean is found in the warm pool of the western equatorial Pacific, where trade winds are weak, atmospheric convection is strong, and precipitation is intermittent and large. On an annual-mean basis, very warm surface water of about 29°C occupies most of the area between 7°N and 10°S, 130°E and 170°W (Kuroda and McPhaden 1993; Levitus 1982; McPhaden and Hayes 1991). The long-term mean wind speed in this region is about 1–3 m s^{-1} (Webster and Lukas 1992), and precipitation is about 4 m yr^{-1} (Taylor 1973). Precipitation over the warm pool exceeds evaporation by 1.5–2 m yr^{-1} (Donguy 1987), which results in relatively low surface salinity 34.5 psu within the pool (Levitus 1982). It is commonly thought that evaporation from the warm pool triggers deep atmospheric convection, which in turn provides a major driving force for the large-scale atmospheric circulation (Philander 1990).

Deep atmospheric convection and heavy rainfall are common over the warm pool during strong westerly winds, which are referred to as ''westerly bursts'' (e.g., Lukas and Lindstrom 1991). Some westerly bursts last a few days, and some last 1–3 weeks with wind speeds greater than 5 m s^{-1} (Keen 1982; McPhaden et al. 1988; Webster and Lukas 1992). A few such bursts with heavy rainfall were observed during the Intensive Observing Period (IOP) of the Tropical Ocean Global Atmosphere (TOGA) Coupled Ocean–Atmosphere Response Experiment (COARE) from various platforms (e.g., Fairall et al. 1996; Short et al. 1997; Weller and Anderson 1996). During the majority of those bursts, precipitation and surface cooling dominated in the surface buoyancy flux (Weller and Anderson 1996).

Near-surface in situ measurements indicate that immediately after heavy rainfall, a low-salinity lens forms at the surface (Paulson and Lagerloef 1993; Soloviev et al. 1993; Soloviev and Lukas 1997). In such a lens, surface mixing is shallow and high values of the dissipation rate of turbulent kinetic energy (ϵ) are limited by a shallow halocline at the bottom of the fresh lens

Corresponding author address: Dr. Hemantha Wijesekera, College of Oceanic and Atmospheric Sciences, Oregon State University, 104 Ocean Admin. Bldg., Corvallis, OR 97331.
E-mail: hemantha@oce.orst.edu

(Brainerd and Gregg 1997; Smyth et al. 1996a,b; Smyth et al. 1997; Wijesekera and Gregg 1996); the lens need not be circular and could be elongated, and its initial structure was probably similar to the rainfall patch, which was complex but elongated (see section 3a). Heavy precipitation can limit the vertical turbulent transport of heat and momentum, thus maintaining a shallow mixed layer in the warm pool (Anderson et al. 1996). Brainerd and Gregg (1997), on the basis of observations and modeling, suggest that rainfall events in the western Pacific warm pool will be mixed away on timescales of a few days, primarily by nighttime convection.

The high degree of spatial and temporal variability of rainfall over the warm pool forces variations in the structure of the oceanic surface layer. Huyer et al. (1997) reported that the thermohaline field was nonstationary and inhomogeneous in the warm pool during the IOP of COARE. They noted that surface mixed layer depths were quite variable, especially during heavy rainfall. Soloviev and Lukas (1997) observed sharp frontal interfaces of width 1–100 m and separation 0.2–60 km in the warm pool. These interfaces were sharpest at the downwind edges of fresh lenses. They suggested that the sharp frontal interfaces could develop by nonlinear evolution of internal waves on the near-surface pycnocline. Smyth et al. (1997) examined temporal variability of mixing behind wakes of rain squalls with wind speeds between 10 and 15 m s^{-1}. During the passage of each squall, a lens of cold freshwater appeared at the sea surface. The rate of turbulent kinetic energy dissipation ϵ within each lens increased by an order of magnitude as wind forcing continued, and values of ϵ below the fresh lens decreased by the same order of magnitude (Smyth et al. 1997).

In this paper we focus our attention on a low-salinity lens caused by heavy rainfall during a westerly wind burst over the warm pool. This freshwater lens, about 20 km across, was sampled at night by two ships on 21 December 1992, while the wind stress was about 0.12 N m^{-2} and the surface heat flux was about 225 W m^{-2} (upward), both nearly constant for a period of several hours. Radar maps indicated that the heaviest rainfall occurred 5–6 h before the ships passed through the low salinity lens. In the following analysis, we investigate the structure and evolution of the low salinity lens by analyzing several surface-layer datasets: temperature and salinity data from bow-mounted sensors and a towed Seasoar vehicle on one ship (R/V *Wecoma*), velocity microstructure data from a freely falling profiler on a second ship (R/V *Moana Wave*), horizontal water velocity measured by acoustic Doppler current profilers on both ships, meteorological data from both ships, and rainfall from ship-mounted radars.

The paper is organized as follows. In section 2, we describe the platforms and instruments used to obtain the data. In section 3, we describe the temperature, salinity, and velocity structure associated with the rain event, which occurred on 21 December 1992 along *Wecoma*'s track. Spectra of temperature, conductivity, and salinity are discussed in section 4. In section 5, we examine mixing in the low-salinity lens by combining both *Wecoma* and *Moana Wave* observations. Gravitational spreading of fresh lenses is considered in section 6. Section 7 summarizes the results.

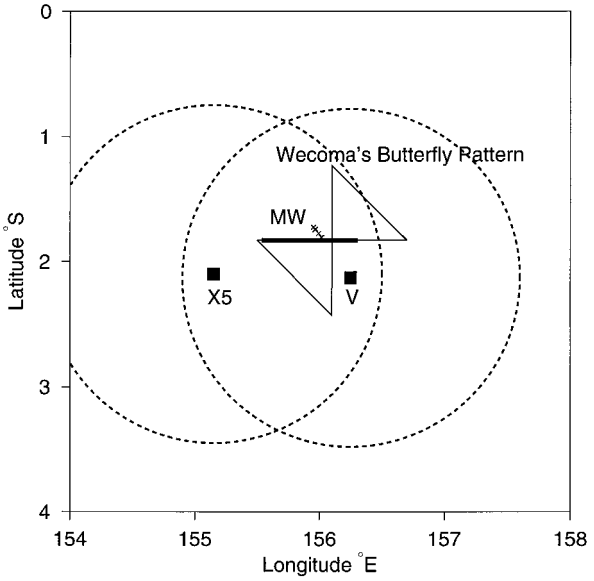

FIG. 1. R/V *Wecoma*'s survey pattern (thin solid line). The thick solid line indicates *Wecoma*'s track between 1300 and 1800 UTC 21 December 1992. Positions of R/V *Moana Wave* are marked as crosses for the same time period. Two dotted circles with radii of 150 km indicate Doppler rain radar coverage, centered at R/V *Xiangyanghong* 5 (X5) and R/V *Vickers* (V).

2. Platforms and instruments

Measurements of surface-layer temperature (T) and salinity (S) were made while the R/V *Wecoma* was steaming in a butterfly pattern (Fig. 1) in the Intensive Flux Array (IFA) during the IOP (Huyer et al. 1997). The zonal and meridional sections of this pattern intersected at 1.83°S, 156.1°E near the nominal position occupied by R/V *Moana Wave* (Fig. 1) (Moum and Caldwell 1994). Measurements of T and S from *Wecoma* were from a Sea-Bird CTD in a vehicle (Seasoar) that undulated in the upper 300 m and from Sea-Bird sensors mounted on an underwater boom, which extended 2 m forward from the bow (Fig. 2). Pressure was also measured on the bow boom, which was at a mean depth of 2 m. Data from the bow boom were recorded on a personal computer at a sampling rate of 8 Hz. At the mean ship speed of 4 m s^{-1}, the spatial sampling rate was 2 cycles per meter (cpm). The sampling rate of the Seasoar CTD was 24 Hz.

Because of the pitching motion of the ship, bow sensors measure T and S at variable depth centered at a mean depth of 2 m. The bow-pressure record revealed

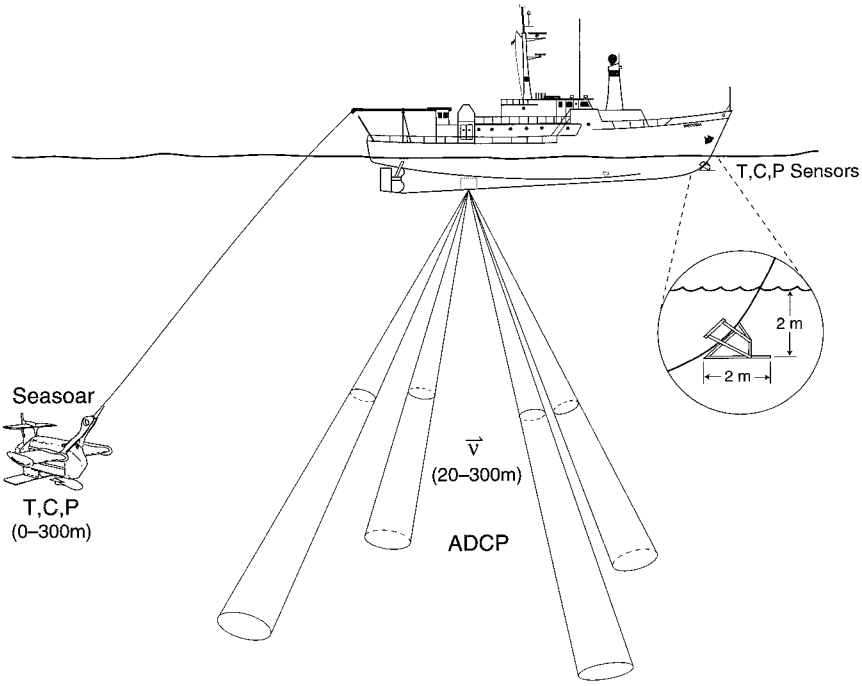

FIG. 2. (a) Schematic diagram of R/V *Wecoma* and measurements. Bow sensors (*T, C, P*) were attached to a bow boom at a depth 2 m below the water level. *Wecoma* was equipped with shipboard ADCP. Seasoar was towed behind the ship. Microstructure measurements were taken from R/V *Moana Wave* (not shown here).

that *Wecoma* pitched at 0.03 Hz with a mean amplitude of 0.6 m, while it was steaming at a speed of 4 m s^{-1} along the east–west transect considered in this paper. High-frequency measurements at 2 m could be contaminated with mean-stratification, especially during heavy rainfall and daytime solar heating. During nighttime winds of 10 m s^{-1}, surface mixing was large and the surface layer was either well mixed or very weakly stratified to at least ~5 m. Therefore the contamination by mean stratification was minimal. If the surface waves are sufficiently large, the bow sensors will come out of the water especially when the ship is headed into the wind. For the analysis here, the *Wecoma* was traveling downwind and the bow sensors were always submerged.

Seasoar measured sawtooth profiles of *T* and *S* in the upper 300 m (Fig. 2); the cycling period was typically 8–12 min, corresponding to a horizontal distance between upcasts of 2–3 km. Temperature, conductivity, and pressure were sampled at 24 Hz, and subsequently processed to provide 1 Hz averages of pressure, temperature, salinity, and density anomaly (σ_t) from ascending profiles (O'Malley et al. 1993; Huyer et al. 1997). Here, we used both 1-Hz data and spatially gridded data (averaged horizontally over 2 n mi along ship's track, and 1 dbar vertically). Most Seasoar profiles used in our analysis include observations in the upper 2 m.

Currents were measured by a 150-kHz, acoustic Doppler current profiler (ADCP) mounted on *Wecoma* (Fig. 2). Average profiles of horizontal velocity were recorded every 5 min (horizontal distance about 1.2 km). The pulse length and bin size were 16 and 8 m. The data was subsequently processed to produce velocity profiles every 10 min in time and every 10 m in the vertical with the top bin centered at 17 m. Each velocity estimate represents an average over 10 min in time and 10 m in the vertical. Horizontal velocity was also measured by a 150-KHz ADCP on *Moana Wave.*

Rainfall was measured on *Wecoma* by siphon gauges, which recorded at intervals of 1 min. The optical rain gauge on *Wecoma* failed prior to the event described here. Other meteorological sensors were mounted at three locations on *Wecoma,* and most instruments recorded at intervals of 1 min; data were subsequently averaged into half-hour means that were used to calculate air–sea fluxes using the COARE bulk flux algorithm (Fairall et al. 1996).

The free-falling microstructure profiler (CHAMELEON) on *Moana Wave* was deployed at intervals of about 10 min (Moum and Caldwell 1994; Smyth et al. 1996a,b). The profiler measures *T* and *S* with a vertical resolution of 0.1 m, and provides estimates of the turbulent kinetic energy dissipation rate (ϵ) for 1-m intervals. The shallowest reliable sample depth was 3 m for temperature and salinity and 10 m for microstructure. In the present analysis, we use 1-m averaged values of *T, S,* density anomaly (σ_θ), and ϵ.

Measurements by two radars were used to estimate rain rate at an altitude of 2 km during the COARE IOP

TABLE 1. Daily averaged surface meteorological measurements from R/V *Wecoma*, R/V *Moana Wave*, and two ship-mounted rain radars: wind speed (U_{10}), wind direction (Dir), wind stress (τ), air temperature (T_{air}), SST, net surface heat flux (Q_{net}: upward flux is positive) from R/V *Wecoma*, rain rate from *Wecoma's* siphon rain gauge (R_{WEC}), *Moana Wave's* optical rain gauge (R_{MW}), and Doppler radar estimates (R_{radar}). The averaged rainfall from *Moana Wave* represents a temporal average (24 h) of rainfall at 1.8°S, 156°E, and that from *Wecoma* represents a time/space (350-km distance for 24-h period) average along the butterfly pattern (Fig. 1). The daily averaged radar rainfall represents time and area (~400 km × 300 km) averages of radar signals, centered near 2°S, 156°E.

Dec (date)	U_{10} (m s^{-1})	Dir (deg)	T_{air} (°C)	SST (°C)	Q_{net} (W m^{-2})	R_{WEC} (mm h^{-1})	R_{MW} (mm h^{-1})	R_{radar} (mm h^{-1})
19	3.21	299	28.8	29.8	−52	0.00	0.35	0.25
20	6.56	304	27.0	29.3	142	0.01	1.94	1.16
21	8.58	310	27.3	29.2	115	0.72	3.53	0.35
22	10.12	279	27.5	29.1	178	0.06	1.27	0.39
23	4.37	290	28.3	29.2	−20	0.0	0.0	0.03

(Short et al. 1997). The measurement area was enclosed by two overlapping circles of 300-km diameter each shown in Fig. 1. The radar data were processed (Short et al. 1997) to provide estimates of rainfall within 2-km square pixels at 10-min intervals.

3. Description of the fresh lens

a. Background meteorology

The observations analyzed here were made during a westerly wind burst in late December 1992. Daily averaged wind stress was small, less than 0.02 N m^{-2}, on both 18 and 19 December. Northwesterly winds began to increase late on 19 December and, though variable, continued to increase until wind stress reached a maximum of 0.3 N m^{-2} at 1800 UTC 22 December. The wind stress then dropped rapidly to 0.03 N m^{-2} by the end of 22 December. Daily averaged wind stresses and net heat fluxes computed from *Wecoma*'s meteorological measurements by use of the COARE bulk flux algorithm (Fairall et al. 1996) for the five days beginning with 19 December are given in Table 1. As shown in Table 1, the strongest surface cooling occurred when winds were largest. The characteristics of this particular westerly wind burst are also described by Weller and Anderson (1997) and by Smyth et al. (1996a,b). There was substantial rainfall associated with the wind burst, although it varied significantly in space and time (Table 1). The largest rainfall estimates were reported from R/V *Moana Wave* near 2°S, 156°E. For example, daily accumulation during 21 December was 85 mm.

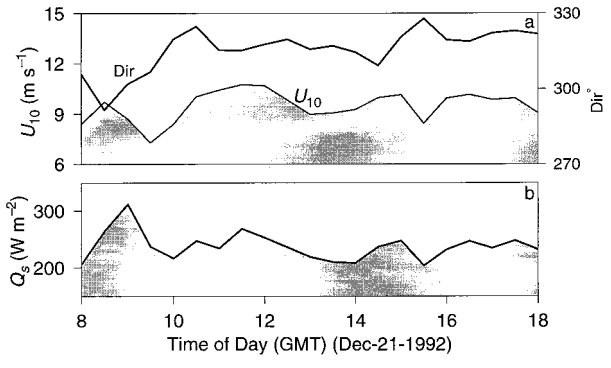

FIG. 3. Near-surface weather data from *Wecoma* for a 10-h segment on 21 December 1992: 30-min averages of (a) wind speed, U_{10} (in m s^{-1}) and direction (solid line), and (b) net surface heat flux (=net longwave radiation + sensible heat flux + latent heat flux + net solar irradiance, in watts per square meter), positive upward.

In this paper we focus on the 10-h period following 0800 UTC 21 December 1992, which encompassed a rainfall event centered at 1100 UTC and the sampling of the oceanic signature of that event some hours later by both *Wecoma* and *Moana Wave*. Wind speed, wind direction, and surface heat flux for the period from 0800 to 1800 UTC are shown in Fig. 3. The wind speed was nearly steady with a mean of about 9.5 m s^{-1}. The mean surface stress during this period was 0.12 N m^{-2}. Wind direction shifted from about 300° at 0800 to a nearly constant 320° from 1000 to 1800 UTC. The mean surface heat flux was about 225 W m^{-2} upward with modest variability. With the exception of rainfall, atmospheric forcing of the ocean was nearly constant from 0800 to 1800 UTC 21 December 1992.

The rainfall field that produced the fresh lens analyzed in this paper is shown in Fig. 4 together with the tracks of *Wecoma* and *Moana Wave*, and the locations of the ships that carried the rain radars. There is a maximum in radar rain rate on the *Wecoma*'s track, which was deposited there about 5 h before its oceanic signature was measured by *Wecoma*. The 1-h averaging interval used to obtain the rain rate in Fig. 4 was chosen to match the time during which rain rate exceeded 10 mm h^{-1} on *Wecoma*'s track. This rainfall pattern illustrates the high degree of spatial variability characteristic of tropical rain rate.

A view of the radar rainfall field as a function of time and space is shown in Fig. 5. Rain rate is contoured as a function of time and longitude along *Wecoma*'s eastward track, which is also shown. The most intense rainfall along *Wecoma*'s track was centered near 155.88°E at 1045 UTC, about 4 h before the ship passed this point. The extent of the most intense rain rate (>10 mm h^{-1}) was 20 km in distance along the ship's track and just over 1 h in time. Within the 10 mm h^{-1} contour (Fig. 5a) the highest rain rate was 100 mm h^{-1} at 155.864°E and 1100 UTC. The average rain rate within the 10 mm

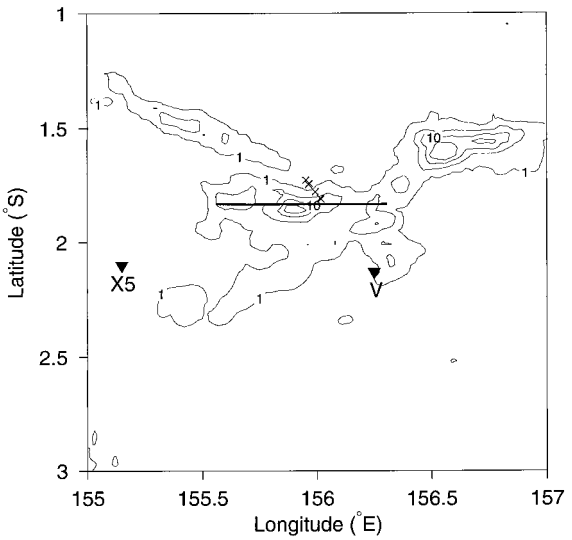

FIG. 4. Rainfall rate (from radar data) averaged over the hour from 1030 to 1130 UTC. The contour levels are 1, 5, 10, and 15 mm h^{-1}. Contour levels 1 and 10 mm h^{-1} are labeled. The horizontal heavy line shows the *Wecoma*'s eastward track from 1300 to 1800 UTC and the crosses show the *Moana Wave*'s southward track for the same period. The triangles show the location of the *Xiangyanghong* 5 and *Vickers,* which carried the rain radars.

h^{-1} contour was 22 mm h^{-1}. The oceanic signature of this event was also sampled by *Moana Wave* from 1600 to 1800 UTC (Fig. 5b), about 2 h after being sampled by *Wecoma.*

We estimated acumulated radar rainfall along *Wecoma*'s track for fixed time intervals (2, 4, 6, and 8 h) preceding the ship's passage (Fig. 6a). It is clear from Fig. 6a that the rainfall that occurred in the 6 h before *Wecoma*'s passage defines a rain accumulation patch centered at 155.88°E.

b. T–S characteristics

The temperature and salinity data from the 2-m bow sensors and the Seasoar data from the upper 60 m along *Wecoma*'s track allow us to describe the general structure of the fresh lens in terms of its surface characteristics, its vertical structure, water mass characteristics, and freshwater content.

Profiles of the 2-m temperature and salinity across the lens show a broad minimum in both *T* and *S* centered on 156.0°E at 1545 UTC (Fig. 6). The width of this minimum (~15 km) is similar to the width of the maximum in rainfall accumulated during the 5 h prior *Wecoma*'s passage, though their positions differed by ~12 km (suggesting eastward advection of the lens; see section 3c below). Within this broad minimum, the small-scale fluctuations of *T* and *S* are highly correlated; this similarity suggests that temperature and salinity are diffusing as passive scalars. The overall trend in temperature, decreasing ~0.1°C between 1300 and 1800 UTC (2300 and 0400 local time) is probably due to the surface cooling, which averaged ~225 W m^{-2} over this period (Fig. 3).

In the subsurface temperature, salinity, and density distributions from Seasoar, the fresh lens appears as a low-salinity, low-density anomaly that extends from the surface to a depth of 40 m (Fig. 7). The fresh lens is also characterized by low temperature in the upper 15 m. This shallow temperature anomaly is underlain by a layer or tongue of warm ($T > 29.3$°C) water that extends from 20-m to 60-m depth under the fresh lens; this warm tongue is almost certainly a remnant of the surface layer that had been warmed by net heating prior to the beginning of the wind burst.

The surface mixed layer depth (SMLD) shown in Fig. 7 is defined as the depth at which the potential density anomaly (σ_θ) exceeds its surface value by 0.01 kg m^{-3} (Peters et al. 1988; Moum et al. 1989). The mixed layer depth defined by this criterion generally coincides with the bottom of the near-surface region of high turbulent dissipation (Peters et al. 1988; Moum et al. 1989; Wijesekera and Gregg 1996; Smyth et al. 1996a,b), but it is important to note that turbulent dissipation may be small within the SMLD, and that dissipation may be large below the SMLD if the vertical shear is large. The SMLD varied between 15 and 50 m over this portion of *Wecoma*'s track (Fig. 7). The surface heat flux and wind stress were nearly steady (Fig. 3), but there are variations in SMLD due to the buoyancy flux associated with rainfall. The shallowest SMLD, about 15–20 m, was found at about 156.0°E within the freshwater lens (Fig. 7). There is a clear association between the density stratification and the amount of rainfall that occurred 4–6 h preceding *Wecoma*'s passage (Fig. 7). The deepest SMLDs were found in regions where there was low rainfall, such as at the end (1800 UTC) of the record.

Temperature–salinity characteristics of the upper ocean evolve with time as rain falls and freshwater mixes into deeper layers. In Fig. 8 *T–S* relations are shown for the edges (1515 and 1610 UTC) and at the middle (1545 UTC) of the lens. The *T–S* curves are similar in shape, although the core of the lens was fresher and colder than the edges (Figs. 7, 8). These *T–S* curves are from ascending Seasoar profiles with a temporal resolution of 1 s and a depth range from 4 to 70 m. In these profiles *T* and *S* have higher vertical resolution in the upper 10 m than at deeper depths because the Seasoar ascent rate slows significantly as it approaches the surface. Near the surface, the ascent rate is typically less than 0.5 m s^{-1}, while the horizontal tow rate continues steady at ~4 m s^{-1}, with the result that *T–S* characteristics can be dominated by horizontal, rather than vertical, variations of *T* and *S.* Interpreting the near-surface curvature of the 1515 UTC characteristic as a vertical profile would suggest that surface waters were hydrostatically unstable, but Fig. 7 shows that the curvature is caused by horizontal variations in *T* and *S*; the Seasoar was being towed nearly horizontally toward the center

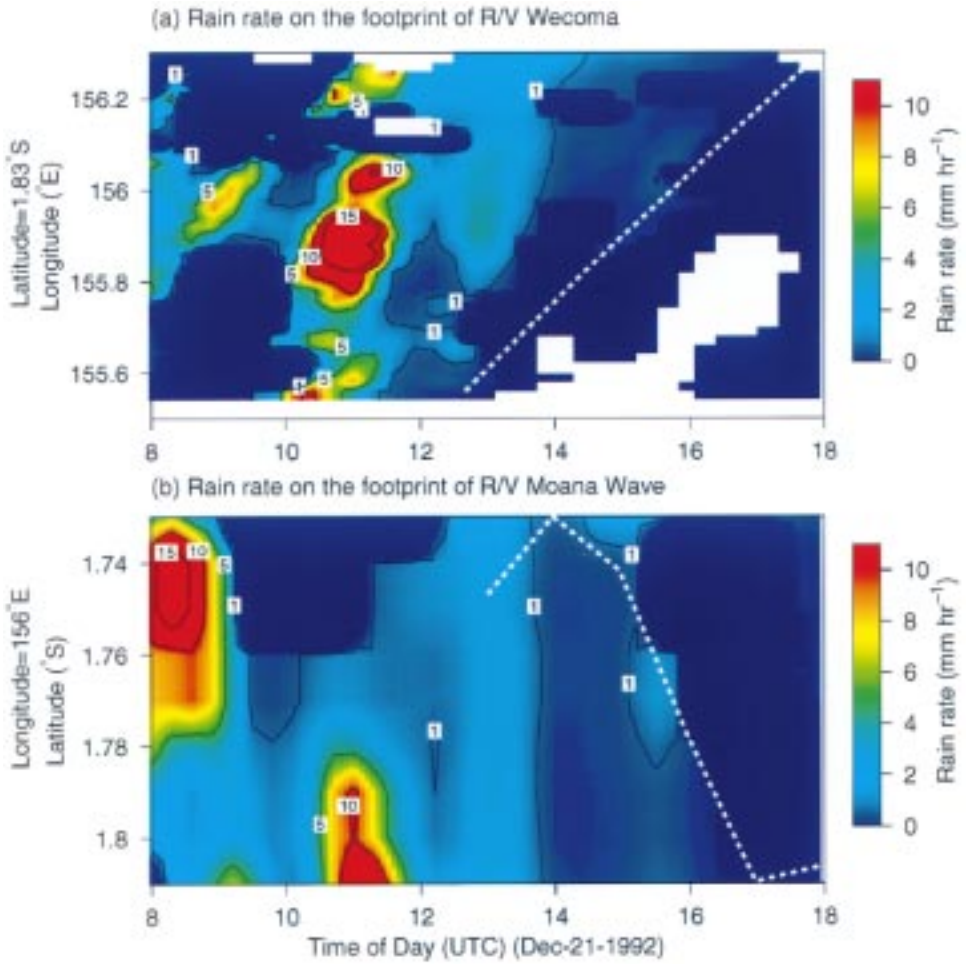

FIG. 5. The distribution of rainfall for 10 hours on 21 December 1992, inferred from radar (Short et al. 1997): (a) along *Wecoma*'s footprint as a function of time and longitude at latitude 1.83°S, and (b) along *Moana Wave*'s footprint as a function of time and latitude at longitude 156°E. Spatial resolution is about 2 km and temporal resolution is 10 min. The thick white dashed lines represent the ship tracks.

of the fresh lens into water with decreasing temperature and salinity.

The general shape of the *T*–*S* relations in the fresh lens (Fig. 8) can be explained as a simple time evolution assuming one-dimensional balances of heat and mass under a constant wind stress of 0.12 N m^{-2} and negligible vertical fluxes below 50 m. Suppose that the initial *T*–*S* relation before rain began to fall has uniform *T* and *S* in the upper 50 m with values given at the observed temperature maximum ($T = 29.34$°C, $S = 34.15$ psu). These values are close to those observed by Seasoar at 50-m depth on 19 December along the same east–west transect, prior to the wind burst. The *T*–*S* relation below 50 m (i.e., where $S = 34.15$ psu) is assumed to be unchanging. When rain begins to fall and other surface heat and mass fluxes are assumed to be zero, the *T*–*S* characteristics of the surface water will lie along the dashed line, shown in Fig. 8, that connects the initial *T*–*S* characteristic with pure rainwater whose salinity is zero and whose temperature is about the same as the wet-bulb temperature (Gosnell et al. 1995), which was observed to be 24.7°C during a rain rate of ~10 mm h^{-1} at a different location on the butterfly during similar wind and surface heat flux values. When the rain stops, the surface cooling (~225 W m^{-2}) tends to cool the surface layer whereas the wind mixing tends to increase its salinity. Hence the *T*–*S* characteristics of the surface layer will move from a point along the dashed line toward lower temperature and higher salinity as observed in Fig. 8. Although Fig. 7 suggests that processes in this case were not strictly one-dimensional and although the observed *T*–*S* relation is undoubtedly the product of several rainfall events since the beginning of the westerly wind burst (Table 1), this basic description of the evolution of the *T*–*S* relation should still be valid so long as there is nearly constant surface cooling and wind stress.

The total rainfall injected into the upper ocean can be estimated from the freshwater anomaly (FWA) between the sea surface and a given isohaline, S_*. This FWA can be expressed as

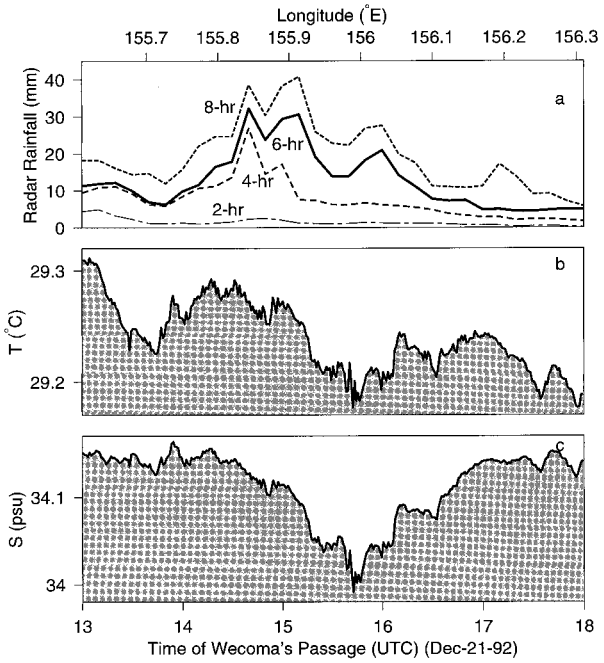

FIG. 6. (a) Accumulated radar rainfall (in mm) for 2, 4, 6, and 8 h preceding *Wecoma*'s passage. (b) 1-min averages, of temperature (T), and (c) 1-min averages of salinity (S) from the bow sensors at 2 m.

$$\mathrm{FWA} = L\left(1 - \frac{1}{L}\int_0^L \frac{S}{S_*}\,dz\right), \tag{1}$$

where L is the depth of S_* (Tully and Barber 1960). We used Seasoar salinity profiles to estimate FWA for several isohalines in the upper 60 m (Fig. 9). High values of FWA associated with the low-salinity lens were located between 155.83° and 156.16°E, with the highest value at 156°E (1545 UTC) where the SMLD was a minimum (Fig. 7). Maximum values of FWA are significantly higher (by a factor of at least 1.5) than maximum values of the accumulated rainfall measured by the radar (Fig. 9). This suggests that the radar may have underestimated the rainfall for this particular event. Feng et al. (1998), who estimated the average rainfall from a freshwater budget for a 19-day period (20 Dec 1992 to 8 Jan 1993), similarly found their rainfall estimate of 15.4 ($\pm$4) mm day^{-1} to exceed the radar rain rate estimate (averaged over the same period and area) by 6 mm day^{-1}, although it agreed with optical rain gauge data within 20%. David Short (1997, personal communication) suggests that attenuation of the radar signal may underestimate true rain rate when rain rates are high (as they were during the event).

c. Horizontal velocity

A westerly wind burst generates an easterly surface current within the equatorial region (Philander 1990), which, in the case considered here, extended south to at least 1.75°S (Smyth et al. 1996a). This eastward current is visible in the ADCP data from *Wecoma* (Fig. 10a), and it is enhanced within the fresh lens (Figs. 6, 7). Inside the fresh lens at 156°E, 1600 UTC, 20-m depth, the eastward velocity (U) and its vertical shear ($\partial U/\partial z$) exceeded 0.35 m s^{-1} and 5 $\times$ 10^{-3} s^{-1}, and anomalies of both velocity and shear extended well below the SMLD (Fig. 10a). The surface velocity would be about 0.5 m s^{-1} if $\partial U/\partial z$ at 20 m remained constant in the upper 20 m. Meridional velocities were small, less than 0.1 m s^{-1} (Fig. 10b).

The direction of the current near the surface (Fig. 10) differed significantly from the direction of the wind vector that produced the current (Table 1). The difference can be ascribed to counterclockwise inertial rotation of the current vector. The direction of the current at 17-m depth, vector-averaged from 1500 to 1800 UTC, was about 100° and the direction of the wind vector averaged for the first two days (20 and 21 Dec) of the wind burst was 127°. The inertial period at 1.83°S is 15.6 days, equivalent to a turning rate of 1 deg h^{-1} for the current vector. The approximate beginning of the wind burst was at 0000 UTC 20 December for a total of 40 h duration before the fresh lens was sampled by *Wecoma*. Hence one would expect that the surface current vector would have rotated about 40° counterclockwise from the wind vector to 87°, which is within 13° of the measured direction at 17-m depth. This is satisfactory agreement, given the uncertainties in measurements and initial conditions. The average current direction for measurement depths between 17 and 47 m was 92°.

The maximum in the 6-h rainfall along the ship's track and the maximum in the FWA observed by the ship were not at the same location (Fig. 9). Near-surface currents, driven by the wind, advected the FWA toward the east during the time interval between formation and observation. The mean zonal advective velocity of the fresh lens can be estimated from the displacement (12 km) and the time interval (5 h) between the rainfall event and the observation of the FWA. The rainfall event was centered at 1050 UTC and 155.9°E. The mean zonal advective velocity of the FWA is estimated to be 0.7 m s^{-1} toward the east with an uncertainty of 0.2 m s^{-1}. The difference in the advective velocity ($\sim$0.7 m s^{-1}) and the extrapolated velocity ($\sim$0.5 m s^{-1}) suggests that the near-surface shear was significantly larger than at 20 m, at early stages, the freshwater lens moved much faster than the speed observed at 20 m, 1600 UTC and it later slowed as the momentum in the freshwater layer mixed with deeper layers.

d. Upwelling and downwelling

Vertical velocity (W) can be estimated by vertically integrating the continuity equation for incompressible flow to obtain

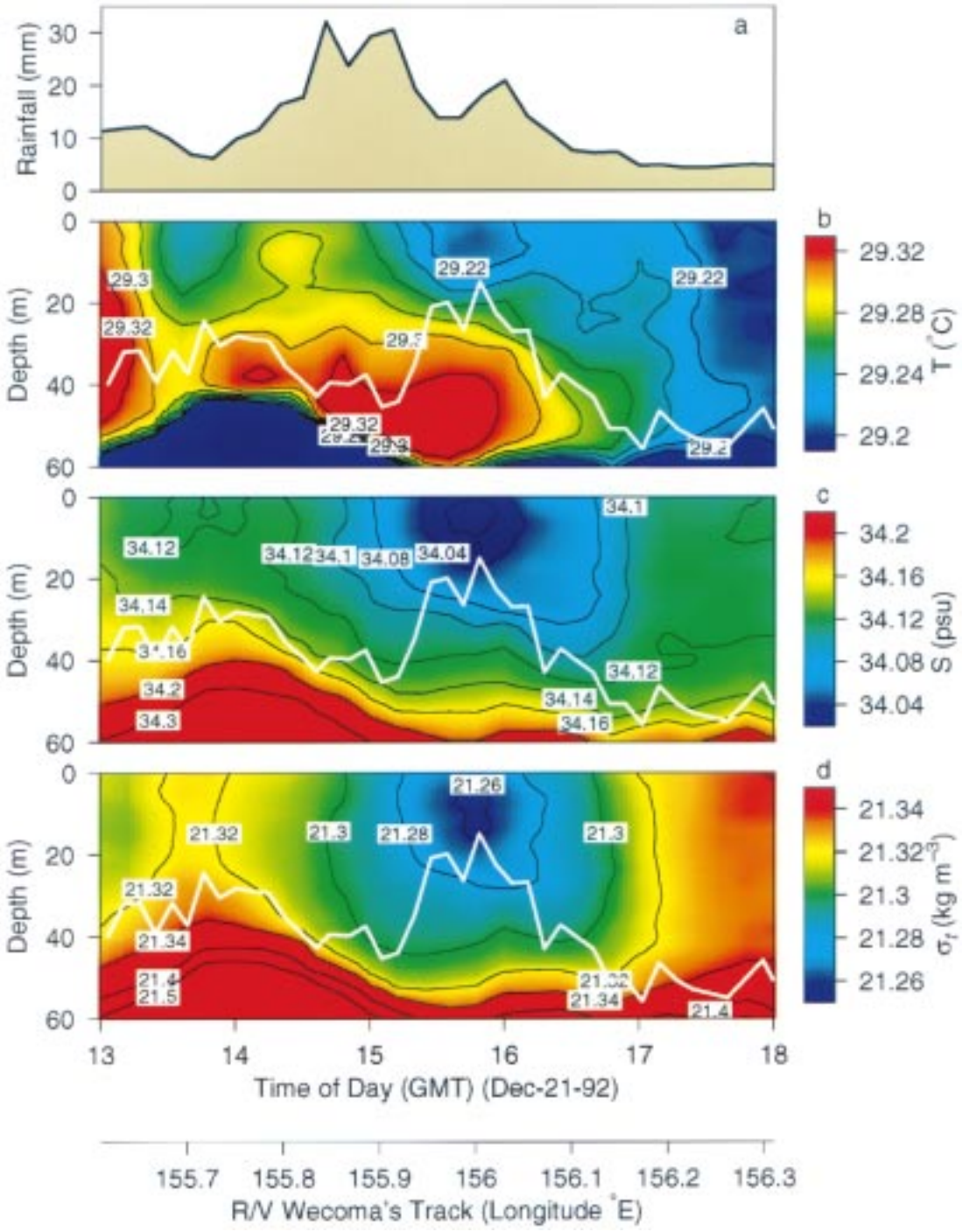

FIG. 7. (a) Accumulated radar rainfall along 1.83°S for the 6 h preceding *Wecoma*'s passage. Near-surface Seasoar distributions: (b) *T*, (c) *S*, and (d) potential density anomaly (σ_θ). The thick white line in each of the lower three panels shows the depth of the surface mixed layer (defined in text).

$$W(z) = -\int_0^z \frac{\partial U}{\partial x}\,dz' - \int_0^z \frac{\partial V}{\partial y}\,dz', \qquad (2)$$

where x is positive eastward, y positive northward, z positive upward with origin at the sea surface, U zonal velocity, V meridional velocity, and the boundary condition $W = 0$ at $z = 0$ has been imposed.

Because we lack measurements of the meridional gradient of V, we cannot estimate the contribution of the second term on the right side of (2) to $W(z)$. However,

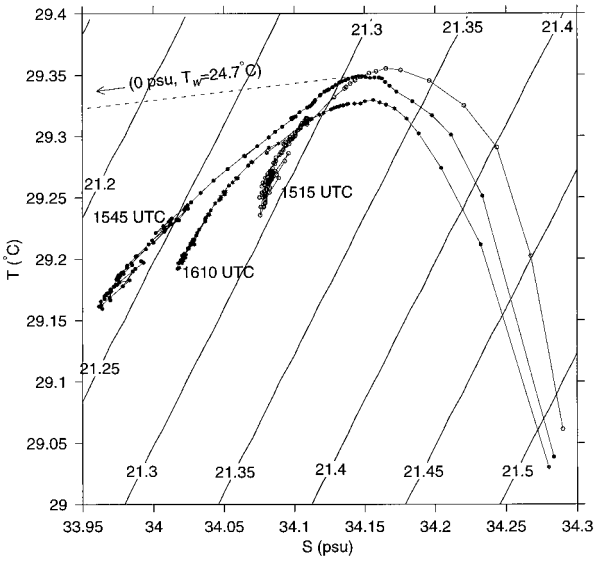

FIG. 8. (a) *T–S* curves for the depth range 4–70 m from three Seasoar profiles at the western edge (1515 UTC), the middle (1545 UTC), and the eastern edge (1610 UTC) of the freshwater lens. The dashed line is directed toward pure rainwater at $T = 24.7°C$, $S = 0$ psu, and represents a possible *T–S* relation during the rainfall.

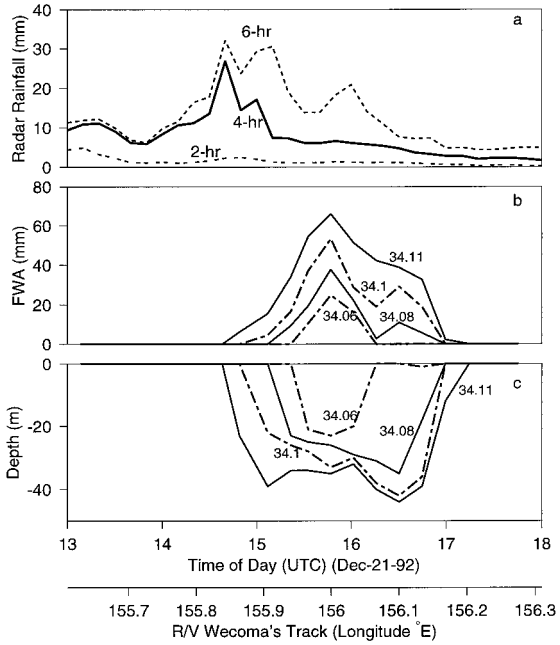

FIG. 9. (a) Accumulated radar rainfall along 1.83°S for the 2, 4, and 6 h preceding *Wecoma*'s passage. (b) Freshwater anomaly (FWA) along 1.83°S calculated from Seasoar salinity data for selected isohalines. (c) The depths of the isohalines selected for calculating FWA.

we argue that the contribution of this term to $W(z)$ is likely to be small in comparison to the first term near the surface and that this contribution may therefore be neglected to obtain an approximate description of near-surface vertical velocity associated with the fresh lens. Because of wind-forcing in the zonal direction, the magnitude of U and its variability near the surface was significantly larger than the magnitude of V and its variability (Fig. 10). Hence, one would expect that the magnitude of near-surface zonal gradients of U would be significantly greater than near-surface meridional gradients of V. One measure of variability is the difference between maximum and minimum values in a time or space series. The maximum minus minimum value of U at 17-m depth for the 5-h period shown in Fig. 10 is 0.38 m s^{-1} and the corresponding difference for V is 0.14 m s^{-1}. It is clear from Fig. 10 that the zonal scale over which the differences occur is approximately the scale of the fresh lens (about 20 km). The ratio of the U and V differences at 17 m is 2.7 and one would therefore expect that zonal gradients of U at this depth would exceed meridional gradients of V by the same factor, assuming that the variability of V in zonal and meridional directions is similar. The ratio of U and V maximum minus minimum differences at depths 27 and 37 m is 2.6 and the ratio decreases to 1.3 and 1.5 at depths of 47 and 57 m, respectively. The validity of neglecting the second term on the right-hand side of (2) is therefore limited to depths of 37 m and above.

Following the argument in the previous paragraph, $W(z)$ was estimated in the upper 40 m from (2) with neglect of the second term on the right side. The first term on the right side was estimated from measurements of zonal velocity shown in Fig. 10; U was measured at 2.4-km (10-min) intervals in the horizontal and at 10-m intervals in the vertical below the uppermost measurement level at 17 m. In carrying out the calculation it was assumed that zonal velocity was uniform above the uppermost measurement at 17 m and that U varied linearly between measurement levels. Zonal derivatives of U were estimated with Δx equal 4.8 km. Calculated vertical velocity is contoured in the lower panel of Fig. 10.

The calculation of W (Fig. 10) shows upwelling at the trailing (upwind) edge of the fresh lens and downwelling at the leading (downwind) edge with peak magnitudes of 20 m day^{-1} at a depth of 20 m. The uncertainty in this estimate of W can be evaluated by considering the second term on the right side of (2) to be an error term and applying the argument from the previous paragraph. If zonal derivatives of U are a factor of 2.6 larger than meridional derivatives of V, the uncertainty in W is $\pm W/2.6$ or $\pm 40\%$. The near-surface upwelling and downwelling extrema at 155.92°E and 156.13°E, respectively, (Fig. 10) are associated with near-zero density stratification in the upper 20 m on the trailing edge of the lens and in the upper 30 m on the leading edge (Fig. 7). The coincidence of near-zero stratification with extrema in W is consistent with the dynamics of upwelling/downwelling, which causes and tends to maintain weak vertical stratification. Conversely, estimates of W below 40 m may not be significant because vertical stratification, which tends to retard vertical motion, is significant in this region (Fig. 7). For

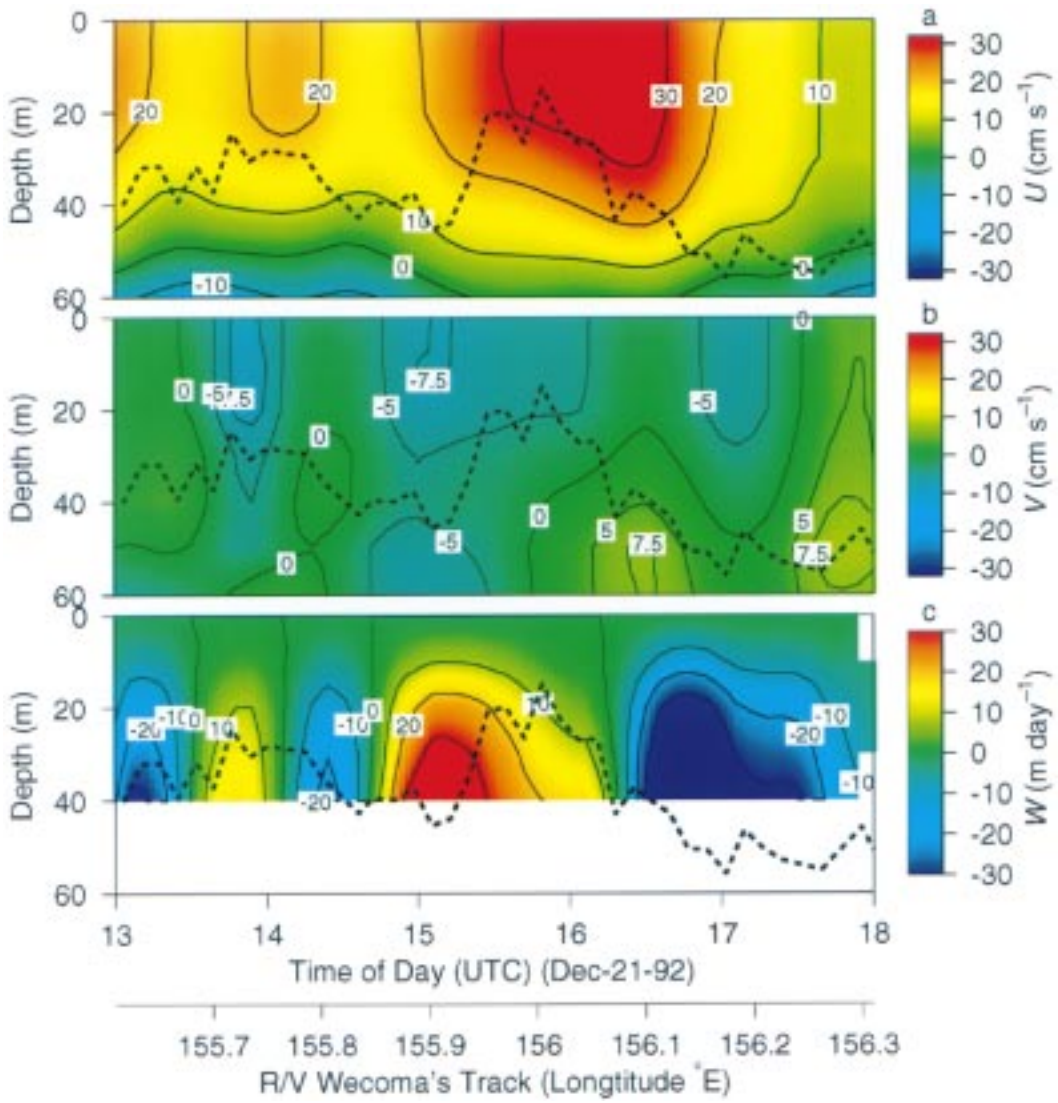

FIG. 10. (a) Time–depth distribution of zonal current *U*, and (b) meridional current *V* from *Wecoma*'s ADCP. The shallowest ADCP bin was at 17 m. In the upper 17 m *U* and *V* were approximated by assuming vertical shears at 22 m remained constant in the upper 22 m. (c) Vertical velocity *W* was estimated by vertically integrating the divergence of zonal velocity. The thick dahsed line denotes SMLD.

this reason, and because both terms on the right side of (2) have similar magnitude below a depth of 40 m, we do not show *W* below 40 m in Fig. 10.

The temperature field associated with the lens (Fig. 7) is consistent with the upwelling/downwelling circulation described above and shown in Fig. 10. At the trailing edge and in the wake of the lens there is a warm temperature anomaly in the upper 20 m that is consistent with upwelling from the warm tongue of water centered at 40-m depth (Fig. 7). At the leading edge of the lens the water temperature is uniformly cold in the upper 20–40 m, which is consistent with downwelling of cold surface water (Fig. 7).

Anderson and coworkers (Anderson et al. 1998; S. Anderson 1998, personal communication) have used a three-dimensional version of the Price–Weller–Pinkel model (Price et al. 1986) to simulate the response of the upper ocean to tropical rainfall, heat flux, and wind stress. The velocity field in the upper 20 m associated with the flesh lenses produced by this model was qualitatively similar to the observations reported here. The extrema in vertical velocity at a depth of 10 m were about 2 m day^{-1} 7 h after the passage of a rain squall. These magnitudes are a factor of 5 smaller than our observations at the same depth (Fig. 10). However, the difference may be accounted for by the fourfold smaller magnitude of the modeled salinity anomaly compared to our observations (Fig. 7) and to weaker model winds (6–7 m s^{-1}) compared to the observations (9–10 m s^{-1}) shown in Fig. 3.

e. Richardson number

A Richardson number was computed from the total shear and the buoyancy frequency N. Total shear, defined by SH $(=[(\Delta U/\Delta z)^2 + (\Delta V/\Delta z)^2]^{1/2})$, was computed from 10-m finite differences of 10 m (vertical) and 10-min averaged ADCP velocity data. The zonal component $\Delta U/\Delta z$ was significantly larger than the meridional component $\Delta V/\Delta z$. Buoyancy frequency was estimated from 10-m differences of 10-m (vertical) averaged σ_θ profiles. Both SH and N were relatively large within the fresh lens near 156°E, 1600 UTC, and these high values extended down to the strongly stratified, high shear region below 50 m (Figs. 11b,c). We combined the gridded ADCP velocity shear and the Seasoar density stratification to compute profiles of 10-m Richardson number (Ri) for every 15-min time interval. Values were close to the critical value of 0.25 in the upper 40 m, consistent with shear-driven mixing in this region (Fig. 11d). These observations suggest that the momentum imparted by wind stress was concentrated in a shallow mixing layer as a result of strong stratification due to rainfall, thus accelerating the mixing layer and generating strong shear and low Ri as shown in Fig. 11.

4. Spectra of temperature, conductivity, and salinity

In this section, we examine spectral properties of temperature, conductivity, and salinity from both 2-m bow data and Seasoar data in the upper 20 m. We describe briefly the methods, limitations, and corrections used in constructing spectra before we discuss their characteristics. An objective of the spectral analysis is to compute dissipation rates of the variances of T and S from the observed T and S spectra, and then to estimate turbulent turbulent fluxes of heat and salt in the upper 10 m.

Coherence and phase spectra of T and S may yield insight into the age of a fresh lens. Before a rain shower, the surface layer is warm and salty. Immediately after a rain shower, surface water is colder and fresher inside the fresh lens than outside because of little mixing and less exposure to downward solar radiation. These fresh and cold anomalies of T and S have high coherence with zero phase over scales decreasing from the size of the rain puddle to the very small scales at which turbulence dominates. However, if a freshwater lens is exposed to downward solar radiation with mixing damped by salt stratification, the temperature of the lens will increase and coherent anomalies of T and S may become 180° out of phase. The effect of random temporal variations in surface heat flux will tend to reduce the initial high coherence between T and S within fresh lenses. Random variations in entrainment of subsurface water into the surface layer will have a similar effect. Hence, as the fresh lens ages, the coherence between T and S will decrease and phase will become random.

a. Bow spectra

Spectra of T, C, and S from the bow-mounted sensors were computed for the period between 1300 and 1800 UTC as a function of wavenumber k, where $k = [U_{\text{wec}} f]^{-1}$ (cpm); $U_{\text{wec}} = 4$ m^{-1} s, is the mean speed of *Wecoma*, and f is the frequency in Hz. Low- and high-wavenumber spectra were computed separately, and then combined to produce the overall spectrum for wavenumbers ranging from 10^{-5} to 1 cpm. A 10% cosine taper was applied to each segment before performing fast-Fourier transforms. Spectra were corrected for effects of the cosine taper. Low-wavenumber ($k < 10^{-3}$ cpm) spectra were computed using the 1-min (240 m) averaged dataset. The length of this data record was about 72 km. For the same record, high-wavenumber spectra were computed for segments spanning 512 s (~2048 m in the horizontal). The high frequency (>1 Hz) rolloff in T was corrected using a frequency domain response function (a double-pole filter, see the appendix for details). The low-frequency (~0.1 Hz) error in C due to thermal-mass of the conductivity cell was corrected using a time domain filter described by Lueck and Picklo (1990) and Morison et al. (1994). A box car response function was used to correct the high-frequency spectral roll off in C. Details of corrections for instrument response are given in the appendix.

b. Seasoar spectra

We also computed spectra of T and S from Seasoar profiles observed between 1300 and 1800 UTC 21 December. The 1-s Seasoar samples correspond to averages over 4 m in the horizontal. As mentioned above, Seasoar sampled the upper 300 m while being towed at a speed of 4 m s^{-1}, thus generating slant profiles of T and S. Seasoar trajectories are approximately horizontal as the surface is approached (Fig. 12a). Each ascending Seasoar profile includes at least 64 data points within the surface layer above 20 m (Fig. 12b); 40 profiles had at least 128 data points in this layer. Spectra were estimated for the top 64 or 128 seconds of each ascending profile.

c. Average spectral characteristics

The spectra of temperature, conductivity, and salinity are red. Spectral slope in the wavenumber range from 10^{-5} to 10^{-3} cpm is approximately -2 (Figs. 13a,b,e), which may be the signature of the mesoscale eddy field (e.g., Samelson and Paulson 1988). At higher wavenumbers (10^{-3}–10^{-2} cpm) spectral slope increases to -1 or greater, then decreases for wavenumbers greater than 10^{-2} cpm. At the highest wavenumbers (10^{-1} cpm), spectral slopes approach $-5/3$, which is characteristic of a turbulent inertial subrange. The existence of a $-5/3$ range is not a sufficient condition for a locally isotropic inertial subrange and turbulence

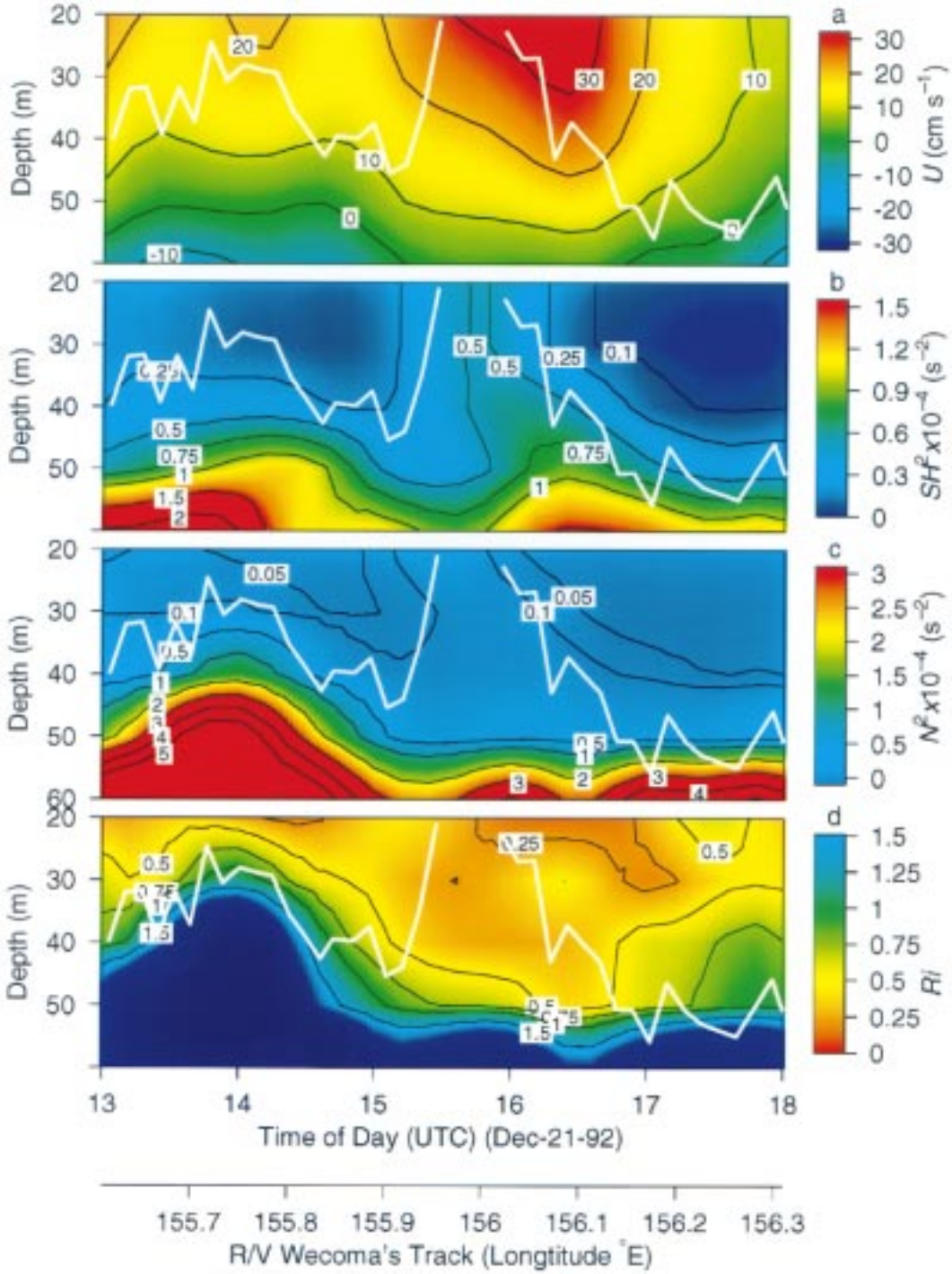

FIG. 11. (a) Time–depth distribution of zonal current (U) measured by *Wecoma*'s ADCP, (b) total shear squared SH^2 ($=[(\Delta U/\Delta z)^2 + (\Delta V/\Delta z)^2]$) from the ADCP, (c) buoyancy frequency squared (N^2) from Seasoar data, and (d) Richardson number (Ri). The thick white line represents SMLD.

measured at a depth of 2 m could not be locally isotropic at a wavelength of 10 m. However, we interpret the existence of a $-5/3$ range as the extension of the spectral slope of a high wavenumber intertial range to lower wavenumbers where the turbulence is not locally isotropic. The decrease in spectral slope to -1 at wavenumbers 10^{-3} to 10^{-2} cpm can be interpreted as the signature of the energy-containing range of near-surface turbulence generated by the wind and the nighttime cooling.

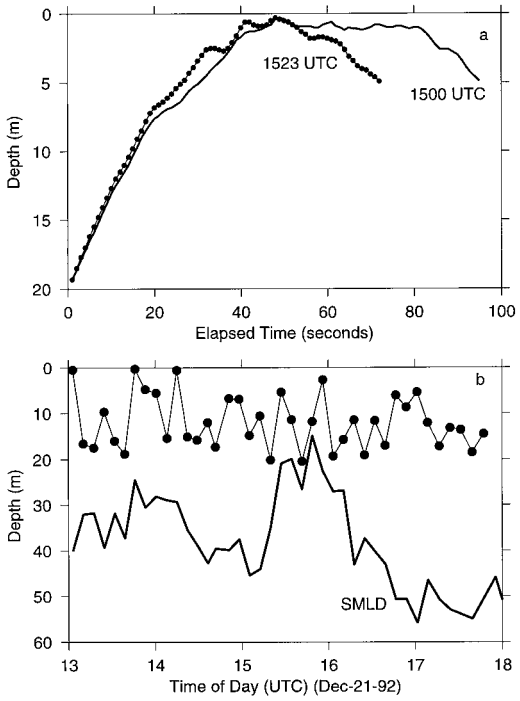

FIG. 12. (a) Typical Seasoar trajectories of ascending profiles as a function of number of data points (or time) in the upper 20 m. (b) The maximum depth of Seasoar data segments, for which temperature and salinity spectra were estimated, are marked with dots joined by a thin line. Each dot represents a separate profile. The thick line represents SMLD. All the data segments were within the surface mixed layer.

d. Spatial variation

High-wavenumber ($k > 10^{-2}$ cpm) spectra of S from the bow sensors show significant spatial variations related to the location of the fresh lens (Figs. 14, 15). The highest salinity spectral levels occur between 1500 and 1600 UTC in conjunction with turbulent mixing within the fresh lens. In contrast, high-wavenumber variations in the spectra of T are small, which may be because turbulent fluctuations of T are generated primarily by nearly constant surface cooling and nearly constant wind stress. The coherence between T and S at 2-m depth varies dramatically with high values associated with the fresh lens (Fig. 14). Phase is close to zero, which is explained by relatively cold rain producing oceanic anomalies, which are cold and fresh. The initial correlation appears to be maintained during the mixing process. Away from the fresh lens, correlation is generally above 0.3 and phase remains close to zero, an indication that salinity fluctuations are primarily caused by recent rainfall, though less intense than the main event.

5. Turbulent mixing

a. Vertical structure

The *Moana Wave* data included routine measurements of microstructure, but these were not available for *Wecoma*. As mentioned earlier, the closest locations of *Wecoma* and *Moana Wave* (while they were in the lens), were 1.83°S, 155.95°–156.05°E (at 1515–1615 UTC) and 1.80°–1.81°S, 156°E (at 1645–1745 UTC), respectively. To examine mixing in the lens, we constructed two sets of 1-h averaged profiles, centered at 1545 and 1715 UTC. For *Wecoma*, a temporal average of 1 h was equivalent to a spatial average of 14.4 km, whereas for *Moana Wave* it was equivalent to 1 km. On average, these two sampling locations were 4 km apart, and *Wecoma* sampled the lens approximately 1.5 h before *Moana Wave*. Thus, we compare the 1545 UTC *Wecoma* profile with the 1715 UTC *Moana Wave* profile (Fig. 16). *Moana Wave* profiles had weaker stratification than *Wecoma*. *Wecoma* data indicate overturning in the upper 10-m (Fig. 16c), but this may be due to aliasing of horizontal gradients into vertical, as Seasoar travels nearly horizontally close to the surface (Fig. 12a). Because of this uncertainty, Seasoar data in the upper 10 m were not used to compute vertical gradients. In both profiles, temperature had a maximum near 50 m (Fig. 16a). The SMLD was about 20 m at 1545 UTC, and it deepened to about 28 m at 1715 UTC (Fig. 16c).

Shown in Fig. 16e is the profile of turbulent kinetic energy dissipation rate (ϵ) from *Moana Wave*; ϵ values in the upper 10 m were excluded because of the contamination by the ship's wake. Dissipation greater than 0.5 to 3 $\times$ 10^{-6} W kg^{-1} (Fig. 16e) was found in the upper 45 m, in which Ri was near critical (Fig. 16d). The largest values of ϵ were found above SMLD, and ϵ decreased with depth as stratification and Ri became large.

b. Turbulent fluxes

Rainfall generates strong salinity stratification at the surface, which in turn decreases the transport of heat and salt into the surface-mixing layer from below. However, strong winds can break down these vertical gradients of θ (or T), S, and σ_θ by turbulent transports across the SMLD, which in turn modify the surface layer. To understand the strength of vertical mixing, we examine turbulent flux profiles inside the lens. We estimate turbulent fluxes in the weakly stratified surface layer by assuming that the turbulent fluxes are proportional to mean gradients such that heat and salt fluxes are written, respectively, as

$$F_\theta = -\rho C_p K_\theta \frac{\partial \theta}{\partial z} \quad [\text{W m}^{-2}] \tag{3a}$$

and

$$F_S = -\rho K_s \frac{\partial S}{\partial z} \quad [\text{kg s}^{-1}\ \text{m}^{-2}], \tag{3b}$$

where ρ is the density, C_p (=4000 J kg^{-1} K^{-1}) is the specific heat of water, and K_θ and K_S are the eddy diffusivities of heat and salinity. The standard way of es-

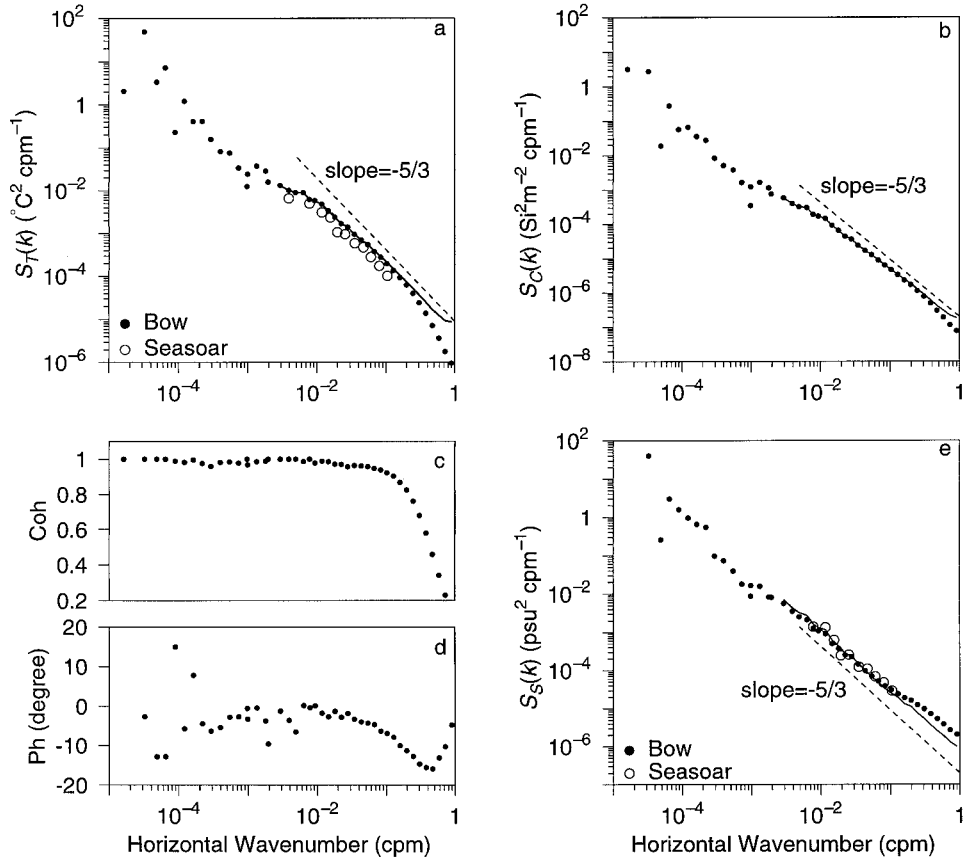

FIG. 13. Averaged-spectral properties. (a) Observed spectrum of T (solid circles) from the bow data, and the corrected spectrum for high wavenumbers (solid line); ensemble-averaged spectrum of T (open circles) from Seasoar measurements. Units are in °C² cpm⁻¹. (b) Observed spectrum of C (solid circles) from the bow data, along with the corrected spectrum for high wavenumbers (solid line). Units are in (siemens m⁻¹)² cpm⁻¹. (c) Coherence between T and C. (d) Phase between T and C; note T lags C. (e) The corresponding salinity spectra from bow data (solid circles) and Seasoar data (open circles). Units are in psu² cpm⁻¹. The solid line denotes the model spectrum from (A3). The $-5/3$ spectral slope is also marked (thin dashed line).

timating eddy diffusivity in the thermocline is either by following Osborn and Cox (1972) or Osborn (1980). Osborn's diffusivity, $K_\theta = K_S = 0.2\epsilon N^{-2}$, is basically limited to the thermocline, where mixing is assumed to be governed by shear instabilities in the flow field. In the unstably stratified mixing layer (where Osborn's technique is not valid), the eddy diffusivity for heat or salinity can be approximated by (Osborn and Cox 1972)

$$K_\phi = \frac{\chi_\phi}{2[\partial\Phi/\partial z]^2} \quad [\mathrm{m^2\ s^{-1}}], \tag{4}$$

where Φ represents either θ or S, and χ_ϕ is the dissipation rate of the variance of Φ. Estimates of χ_ϕ are needed to evaluate scalar fluxes using (3). Accurate measurements of χ_ϕ were not available inside the lens, and therefore χ_ϕ was estimated indirectly from the inertial subrange of the observed scalar spectrum following Monin and Yaglom (1975):

$$\chi_\theta = \frac{\epsilon^{1/3}}{\beta(k_2 - k_1)} \int_{k_1}^{k_2} k^{5/3} S_\phi(k)\, dk, \tag{5}$$

where $S_\Phi(k)$ is either the temperature or salinity spectrum, β (=0.5) (Monin and Yaglom 1975; Williams and Paulson 1977) is the universal constant for the one-dimensional scalar spectrum, k is the wavenumber in reciprocal meters, and k_1 and k_2 are the lower and upper limits of the integration, respectively. We selected $k_1 = 0.05 \times 2\pi$ and $k_2 = 0.6 \times 2\pi$ m^{-1} for bow spectra in which the inertial-subrange spectral levels, $k^{5/3}S_T(k)$ and $k^{5/3}S_S(k)$ were independent of k (Fig. 17). Within the freshwater lens, the spectral level of $k^{5/3}S_T(k)$ and $k^{5/3}S_S(k)$ at 2 m and in the upper 20 m were comparable. Because of the availability of dissipation measurements and the applicability of the standard microstructure techniques, we evaluate F_θ and F_S for three different vertical segments: at 2 m, between 10 and 20 m, and below the SMLD (~28 m).

1) At the depth of 2 m

There were no direct measurements of ϵ or χ at this depth, and furthermore, accurate estimates of $\partial S/\partial z$ and

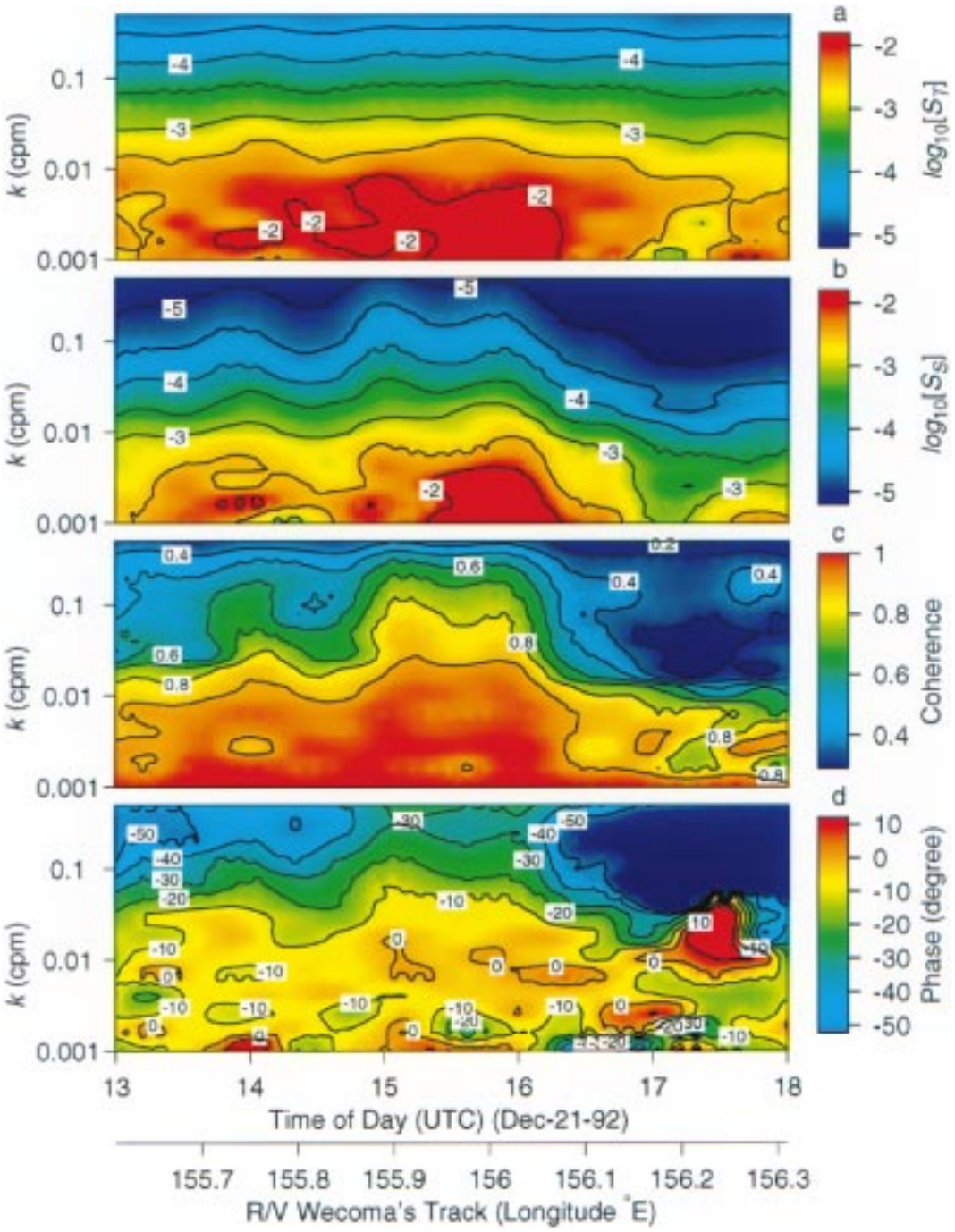

FIG. 14. Horizontal-wavenumber spectra along *Wecoma*'s track from the bow-mounted (2 m) sensors along with accumulated radar rainfall: (a) temperature (in °C^2 cpm^{-1}), (b) salinity (in psu^2 cpm^{-1}), (c) coherence between T and S, and (d) phase between T and S (in degrees). Note T lags S.

$\partial\theta/\partial z$ were not obtained from either Seasoar or bow-mounted sensors. Therefore, the Monin–Oboukhov similarity theory was used to assess the heat flux at 2 m. Similarity theory applies to a surface layer in which the heat flux is approximately constant (Businger et al. 1971) within the surface layer. First, we computed ϵ and χ_θ from the similarity formulations (6a,b) (see below). Then a consistency check was made by comparing χ_θ from the similarity method (6b) with χ_θ from the inertial dissipation method (5). Note that our estimate of χ_θ from the inertial dissipation method was not completely independent from the similarity method because of the

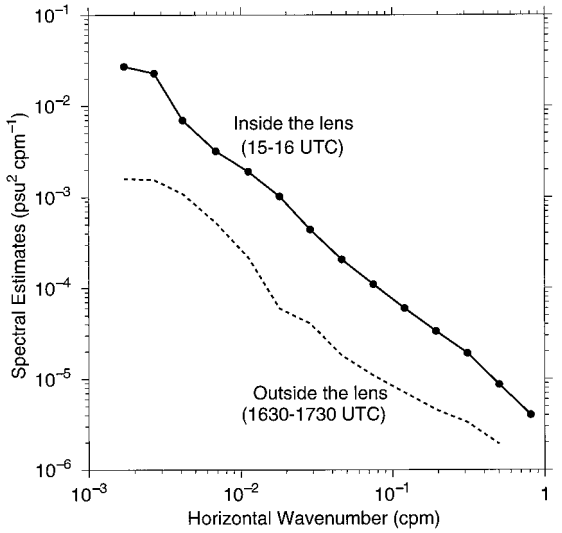

FIG. 15. Spatial variability in salinity spectra. Observed spectra of salinity (solid line with bullets) inside the freshwater lens (1500–1600 UTC) and outside the lens (dashed line) (1630–1730 UTC).

weak dependence on ϵ (5). The dissipation rates of temperature variance (θ^2) and turbulent kinetic energy can be written in terms of universal functions as (e.g., Businger et al. 1971)

$$\chi_\theta = \left| 2\frac{u_* \theta_*^2}{k_z} \phi_\theta(\xi) \right| \tag{6a}$$

and

$$\epsilon = \left| \frac{u_*^3}{\kappa z} \phi_\epsilon(\xi) \right|, \tag{6b}$$

where $\xi = -z/L_O$ is the stability parameter, $\theta_* = Q_s[\kappa\rho u_* C_p]^{-1}$ is the similarity scale for temperature, $u_* = (\tau/\rho)^{1/2}$ is the friction velocity, $L_O = -u_*^3[\alpha g Q_s/\kappa\rho C_p]^{-1}$ is the Monin–Oboukhov length scale, $\kappa = 0.4$ is the von Kármán constant, $g = 9.81$ m s^{-2} is the acceleration of gravity, and $\alpha \approx 3 \times 10^{-4}$ °C^{-1} is the coefficient of thermal expansion. The vertical coordinate z is positive upward. For $Q_s = 225$ W m^{-2}, and $\tau = 0.12$ N m^{-2} (Fig. 3), $L_O = -18$ m and the resulting universal functions ϕ_θ and ϕ_ϵ for $\xi < 0$ are (Businger et al. 1971; Paulson et al. 1972)

$$\phi_\theta(\xi) = (1 - a\xi)^{-1/2}$$
$$\phi_\epsilon(\xi) = (1 - b\xi)^{-1/4} - \xi, \tag{7}$$

where the constants a and b were set to 16, similar to the values used in the COARE bulk air–sea flux algorithm (Fairall et al. 1996).

The similarity theory predicts ϵ, χ_θ, $\partial\theta/\partial z$, and K_θ to be about 2×10^{-6} W kg^{-1}, 4.1×10^{-7} °C^2 s^{-1}, -3.6×10^{-3}°C m^{-1}, and 1.6×10^{-2} m^2 s^{-1}, respectively. As shown in Fig. 17, the estimate of χ_θ from the inertial dissipation method (5), is consistent with the prediction from similarity theory, suggesting that the heat flux at 2 m is similar to the surface value. The estimated χ_s from the salinity spectrum was about 1×10^{-7} psu^2 s^{-1} (Fig. 17). Finally, we computed the turbulent flux of salt from $F_S = \rho(\chi_S/\chi_\theta)^{1/2} F_\theta$, where $K_\theta = K_S$. The estimated diffusivities and fluxes are plotted in Figs. 18a–d.

Heat fluxes inside and outside the lens were expected to be similar because surface cooling, wind stress, and spectral levels of temperature at 2 m were approximately independent of x. However, small-scale variability in salinity was not steady in space and time due to intermittent rainfalls. The smallest variability in salinity was found after 1630 UTC, when the spectral level of salinity was one order of magnitude smaller than inside the lens (Figs. 14, 15). Outside of the fresh lens, intermittent light rainfall and evaporative cooling were the only surface forcing mechanisms that generated near-surface salinity fluctuations. Evaporative cooling of 150 W m^{-2} can generate a downward salt flux of about -0.2×10^{-4} kg s^{-1} m^{-2}, which is one order of magnitude smaller than fluxes inside the lens and is similar to the flux at a depth of 2 m outside the lens (Fig. 18d).

2) BETWEEN 10 AND 20 m

We used the Osborn and Cox (1972) procedure (3, 4, and 5) to compute both F_θ and F_S from 10-m averages of $\partial\theta/\partial z$, $\partial S/\partial z$, ϵ, χ_θ, and χ_S. There is some uncertainty associated with χ_θ and χ_S because of the 1.5-h time lag between *Moana Wave* and *Wecoma* measurements. Since the scalar dissipation rate is proportional to $\epsilon^{1/3}$ (as given in 4), we would not expect large uncertainties in fluxes due to the intermittency of ϵ. For example, if two measurements of ϵ at 1545 and 1715 UTC differed by a factor of 10 (which is most unlikely), then the scalar dissipation rates would be within a factor of 2.

3) BELOW SMLD

Below SMLD (>28 m), flux profiles of heat and salinity were constructed using Osborn's (1980) diffusivity from *Moana Wave* observations. Four-meter averages of ϵ, $\partial\theta/\partial z$, and $\partial S/\partial z$ were used in this computation. The estimated K_θ (or K_S), F_θ, and F_S, along with 95% confidence limits from the bootstrap method are illustrated in Fig. 18.

4) COMBINED FRESH LENS PROFILES

The combined TKE dissipation rate, eddy diffusivity, and fluxes are shown in Fig. 18. At the SMLD, the eddy diffusivity was as high as 2×10^{-2} m^2 s^{-1}, decreased rapidly with depth, and became negligible ($\sim 10^{-5}$ m^2 s^{-1}) below 50 m. The heat flux (F_θ) was upward in the upper 40 m, where $\partial\theta/\partial z < 0$ (Figs. 16a, 18c), and was within a factor of 2 of the heat flux at the surface (Fig. 18c); F_θ was small and downward below 50 m, where

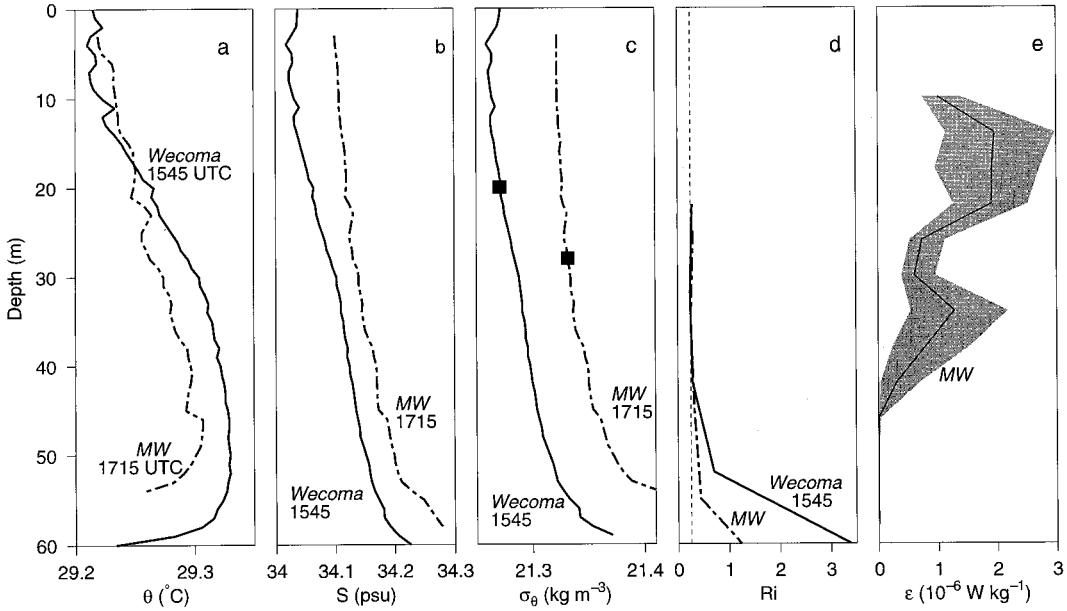

FIG. 16. (a) One-hour-averaged hydrographic profiles in the low-salinity lens from two platforms. Solid line denotes averages made at 1515–1615 UTC from *Wecoma*, and dashed line denotes averages made at 1645–1745 UTC from *Moana Wave*: (a) potential temperature (in °C), (b) salinity (in psu), (c) potential density anomaly (kg m^{-3}) along with SMLD (solid squares), (d) Richardson number (the thin dashed line represents Ri = 0.25), and (e) turbulent kinetic energy dissipation rate ϵ (in watts per kilogram) measured from the *Moana Wave* along with 95% confidence limits from the bootstrap method (shaded areas).

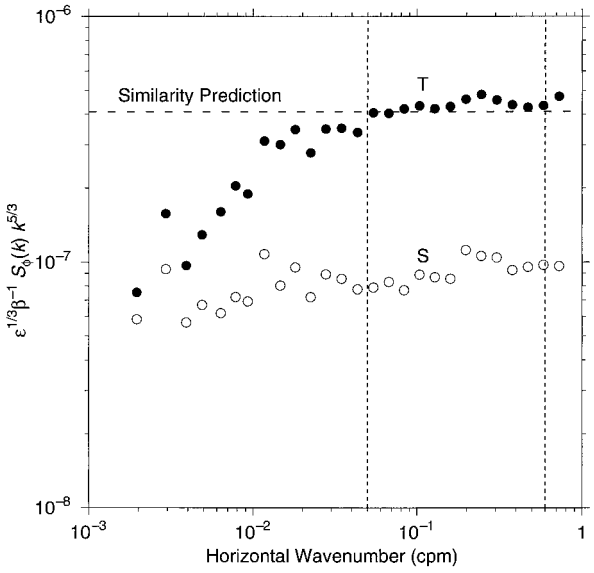

FIG. 17. Scaled spectrum of T (solid circles) (in °C^2 s^{-1}), and scaled spectrum of S (open circles) (in psu^2 s^{-1}) at 2 m, averaged over the freshwater lens. The scaled spectrum, $\epsilon^{1/3}\beta^{-1}k^{5/3}S_\phi(k)$, provides the magnitude of the scalar dissipation rate (5), where ϵ is turbulent kinetic dissipation rate at 2 m based on the similarity theory (6b), and the universal constant, $\beta = 0.5$. The distance between two dashed lines denote the wavenumber band over which χ_θ and χ_S were estimated. The prediction of χ_θ from the similarity theory (6a) is also marked.

$\partial\theta/\partial z$ was large and positive, and ϵ was small. The upward salt flux (F_S) was nearly constant in the upper 20 m, was largest just below SMLD, and decreased rapidly with depth below 40 m (Fig. 18).

By assuming that the eddy diffusivity K_θ at the SMLD remained approximately steady during early evolution of the freshwater lens, we can estimate the timescale of deepening (t_d) of the mixing layer as SMLD$^2/K_\theta$. For $K_\theta \approx (1\text{–}2) \times 10^{-2}$ m^2 s^{-1}, and SMLD = 15–20 m, t_d is 3–11 h, which is compatible with the observations (Figs. 5a, 7). We conclude that during winds of 10 m s^{-1}, the lifetime of a fresh lens is limited to less than a day. In the presence of strong winds, turbulent entrainment plays an important role by transporting heat and salt vertically upward, thus reducing both horizontal and vertical patchiness created by the rainfall.

6. Gravitational spreading

Another way of decreasing a low-density (or a low-salinity) anomaly is by horizontal dispersion, rather than by vertical diffusion. The horizontal dispersion of fine-scale fronts (that were generated by rainfall) in the warm pool was discussed by Soloviev and Lukas (1997). They suggested that some rain-generated salinity fronts can be described as a nonlinear buoyant adjustment of near-surface stably stratified layers to external forcing (such as buoyancy flux and wind stress). An internal bore model (e.g., Barenblatt and Shapiro 1984) was used to describe some aspects of frontal dynamics. The model

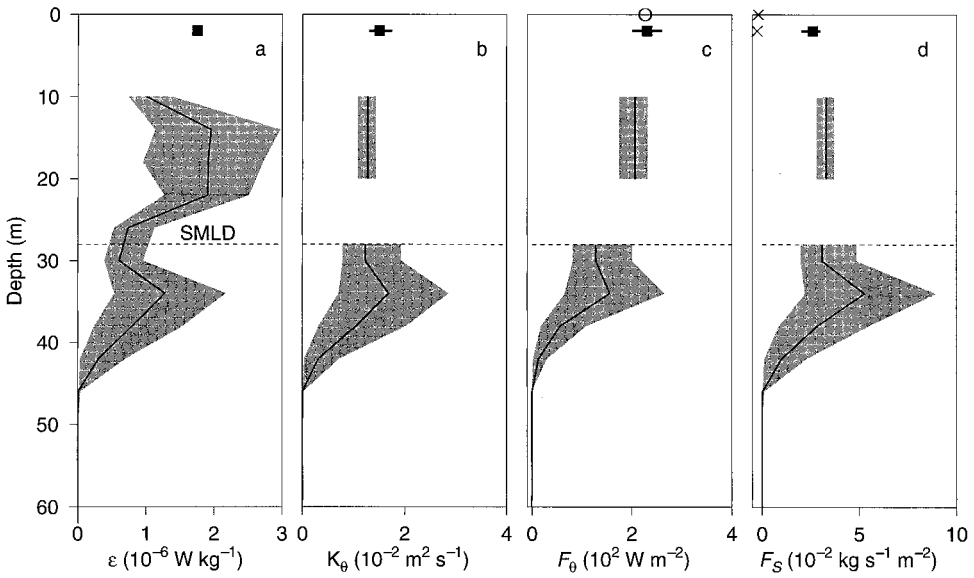

FIG. 18. One-hour-averaged profiles in the low-salinity lens. The thin dashed line denotes SMLD at 1715 UTC. Solid squares represent mixing parameters at 2 m from the similarity method. (a) Turbulent kinetic energy dissipation rate ϵ measured from the *Moana Wave* along with 95% confidence limits from the bootstrap method (shaded areas); the solid square denotes ϵ at the depth of 2 m from the similarity method. (b) Eddy diffusivity: at 2 m from the similarity theory (solid square), between 10 and 20 m from Osborn and Cox (1972), and below SMLD from Osborn (1980). (c) Heat flux, F_θ, and (d) salt flux, F_S. The open circle ("○") in Fig. 18c denotes the surface heat flux of 225 W m^{-2}. The crosses ("×") in Fig. 18d denote salt fluxes outside the lens at 1700 UTC: at the surface (based on 150 W m^{-2} of evaporative cooling) and at 2 m (based on the inertial-dissipation method).

predicts that an initially smooth disturbance evolves into a dissipative shock-wave structure if a governing flow parameter, $\mathrm{Re}_* < \mathrm{Re}_{cr}$ (=2.74), where $\mathrm{Re}_* = h(g'h)^{1/2}/K_m$, h is height of the density anomaly ($\Delta\rho$), K_m is the eddy viscosity, and g' ($=g\Delta\rho/\rho$) is the reduced gravity. For $\mathrm{Re}_* > \mathrm{Re}_{cr}$, the initial disturbance evolves into a series of solitons (i.e., a wavelike dispersive solution; Soloviev and Lukas 1997).

We applied this buoyant spreading scenario to our low-salinity lens to examine possible dynamical processes that might be important after 6 hours of strong winds and surface cooling. For h = 20 m, $\Delta\rho$ = 0.01–0.02 kg m^{-3} (Figs. 7d, 16c), K_m ($\approx \epsilon/SH^2$) = (2–5) × 10^{-2} m^2 s^{-1} (Figs. 11b, 18a), Re_* is 17–70, suggesting a wavelike dispersive solution. If the density anomaly propagated like a solitary wave train (as predicted by the model), then an approximate propagation speed, $(g'h)^{1/2}$ would be about 0.05 m s^{-1}, about 25% of the observed anomaly (~0.2 m s^{-1}) in horizontal velocity inside the lens (Fig. 10a). Therefore, during strong winds, gravitational spreading is not an important process for smoothing out the rain-produced buoyancy anomaly.

7. Conclusions

We have studied some characteristics of a fresh lens in the western equatorial Pacific during the IOP of TOGA COARE. The 7-h period encompassing formation of the lens and in situ measurements coincided with a westerly wind burst with wind out of the northwest at 10 m s^{-1} and with nighttime surface cooling of 225 W m^{-2}. The lens was about 20 km across based on radar rainfall measurements and on a *T–S* section across the lens 5 h after it was formed. The rainfall that formed the lens lasted for about an hour with an hourly accumulation of 20–30 mm from the radar measurements. The fresh lens was sampled 5–6 h after the rainfall by *Wecoma* and *Moana Wave*. The combined analysis of temperature, salinity, velocity, microstructure, and rainfall measurements led to the following results:

1) In the 5 h following its formation, the low-salinity anomaly deepened to 40 m with a surface magnitude of 0.12 psu. The surface magnitude of the corresponding rain-induced temperature anomaly was 0.05°C. The coherence of *T* and *S* within the anomaly was high, with zero phase, which is consistent with initial formation by cold rainfall.
2) The maximum freshwater anomaly within the lens was about twice the accumulated rainfall estimated from the radar.
3) The *T–S* relation of the fresh lens did not lie along the straight line connecting the properties of the upper ocean before the rainfall with the *T–S* properties of the rainfall. The curvature of the *T–S* relation can be explained by surface cooling and mixing subsequent to rainfall.

4) The *T*–*S* anomaly coincided with an anomaly (0.2 m s^{-1} magnitude at a depth of 20 m) in horizontal velocity toward the east (40° to the left of the wind velocity vector). The enhanced velocity of the fresh lens is consistent with trapping of momentum flux from the wind in the upper layers due to rain-induced stratification. The difference in direction between the wind and water velocity vectors can be explained by inertial turning of the water velocity vector. Velocity was not measured directly in the upper 17 m, but the fresh lens was displaced toward the east from the location of the rainfall event by an amount consistent with a mean advective velocity of 0.6 m s^{-1}. This observation further supports the concept of momentum trapped near the surface by rain-induced stratification.
5) Vertical velocity estimated from the divergence of zonal velocity shows downwelling at the downwind edge of the lens and upwelling at the upwind edge. Magnitudes at 20-m depth are 20 m day^{-1} ± 40%.
6) The Richardson number was low within the lens, 0.25–0.5 down to a depth of 40 m, which suggests that turbulent mixing within the stratified lens was governed by critical-Ri instability.
7) Wavenumber spectra of scalar fields (*T, C,* and *S*) in the upper 20 m exhibit a −5/3 range that extends to wavenumbers below the range of local isotropy. The spectral levels in the −5/3 range were used to estimate turbulent dissipation rates of *T* and *S,* which were in turn used to estimate the turbulent fluxes of heat and salt.
8) The similarity method and the inertial dissipation method yielded similar estimates of heat flux at a depth of 2 m, which were similar to the surface heat flux. The estimated turbulent heat and salt fluxes within the lens in the upper 40 m were 100 to 250 W m^{-2} (upward) and 2×10^{-2} to 6×10^{-2} kg s^{-1} m^{-2} (upward). The turbulent diffusivity in the upper 40 m was 1×10^{-2} to 2×10^{-2} m^2 s^{-1}. Fluxes were negligible below 45-m depth.
9) The low-salinity water penetrated to 40-m depth within 5 h, suggesting that the lifetime of fresh lenses is less than one day during westerly wind bursts.

Acknowledgments. We gratefully acknowledge COARE collaborators Roger Lukas, Peter Hacker, Eric Fring, and Mike Kosro who participated fully in cruise planning and data collection. We thank Robert O'Malley and Jane Fleischbein for processing Seasoar data, Lynn deWitt and Fred Bahr for archiving and processing bow data, Eric Firing for providing *Wecoma* ADCP data, and Bill Smyth and Jim Moum for providing *Moana Wave* microstructure and hydrography data. We are also grateful to *Wecoma* Marine Technicians Marc Willis, Brian Wendler, Mike Hill, and Tim Holt for successful operation of the Seasoar system and bow-mounted systems, and *Wecoma*'s crew for their support at sea. Discussion of radar rainfall with Paul Kucera is greatly appreciated. We thank David Short, Bill Smyth, Alexander Soloviev, and two anonymous reviewers for helpful comments and suggestions. This work was supported by the Ocean Science Division of National Science Foundation Grants OCE-9113510, OCE-9319892, and OCE-9525858.

APPENDIX

Construction of Bow Spectra

The autospectrum of raw *T* and the coherence spectrum between raw *T* and raw *C* roll off rapidly at higher wavenumbers, starting from 0.2 cpm (0.8 Hz) (Figs. 13a,c), as a result of frequency responses of *T* and *C* sensors. The spectrum of *C* rolls off less rapidly than that of *T* (Figs. 13a,b). This discrepancy is primarily due to the difference in response times of the *T* and *C* sensors, and these frequency response functions must first be determined to correct the spectra.

a. Temperature response

To correct for the finite time constant of the temperature sensor (fast response Sea-Bird sensor, SBE3), a frequency domain correction was applied to raw spectral estimates of *T,* using a two-pole filter, $F(f) = [1 + (2\pi\tau f)^2]^{-2}$, where τ is the response time of the thermistor in seconds, and f is sampling frequency in Hz (Gregg et al. 1973; N. Larson 1996, personal communication). The response time, τ is a strong function of flow speed, V_f, and follows a power law, $\tau \approx aV_f^b$, where *a* and *b* are constants (e.g., Gregg et al. 1973; Gregg et al. 1978; Lueck et al. 1977). For $V_f = 1$ m s^{-1}, τ is 0.072 s, and $V_f = 0.5$ m s^{-1}, τ is 0.084 s (Sea-Bird Electronics, Inc., Bellevue, Washington), and *a* and *b* become 0.072 and 0.222. For $V_f = 4$ m s^{-1}, the speed of *Wecoma* moving through the water, τ becomes 0.0633 s. It is clear from Fig. 13a that the corrected spectrum basically recovered most of the signal.

b. Conductivity response

Time- and frequency-domain corrections were applied to the conductivity data and spectra, respectively: one correction (frequency-domain) for the response time of *C* and another (time domain) for the thermal mass of *C* cell. Both of these corrections require the flow speed through the conductivity cell, which is not necessarily the same as the speed of the sensor through the water. During this experiment, the bow conductivity sensor was operated without using a standard Sea-Bird pump. As suggested by N. Larson, (1997, personal communication), at a ship speed of 4 m s^{-1}, flow speeds in the cell would be about to 1 m s^{-1}. First, we applied the time domain correction due to thermal inertia of the conductivity cell (SBE4) by following Lueck and Picklo (1990) and Morison et al. (1994). Since our measure-

ments were from the surface mixed layer, where there were no large vertical gradients, this correction was almost negligible. To correct for the finite time constant of the conductivity sensor, a frequency domain correction was applied to raw spectral estimates of C. The conductivity cell produces a box-car average, and therefore, the first order response of C can be approximated as $F_{bc} = \sin(2\pi f\tau_c)/2\pi f\tau_c$, where $\tau_c = 1.25/(17.485V_c)$ (Gregg and Hess 1985; N. Larson 1997, personal communication), where V_c is the flow speed through the cell; for $V_c = 1$ m s^{-1}, τ_c becomes 0.071 s. Both the corrected and raw spectra are given in Fig. 13b.

c. Modeled salinity spectrum

The raw salinity spectrum tends to flatten at higher wavenumbers (Figs. 13e, 15), thus limiting the resolution to about 0.1 cpm. As we discussed earlier, both raw T and raw C spectra roll off at higher wavenumbers, which in turn modified the salinity spectrum. Conductivity is a function of both T and S (Fofonoff and Millard 1983), and therefore, salinity fluctuations (S'), and its variance (S'^2) can be approximated, respectively, as

$$S' = -\alpha_1 T' + \alpha_2 C' \tag{A1}$$

$$S'^2 = \alpha_1^2 T'^2 + \alpha_2^2 C'^2 - 2\alpha_1\alpha_2 C'T', \tag{A2}$$

where $\alpha_1 = (\partial S/\partial T)_C$, and $\alpha_2 = (\partial S/\partial C)_T$, and prime denotes fluctuations. Assuming a perfect correlation between T and C, we write the spectrum of salinity, Φ_S, as

$$\Phi_S = \alpha_1^2\Phi_T + \alpha_2^2\Phi_C - 2\alpha_1\alpha_2\Phi_{CT}, \tag{A3}$$

where Φ_T, Φ_C, and Φ_{CT} are autospectrum of T, autospectrum of C, and cospectrum of T and C, respectively. In the inertial subrange turbulence, where there is no production or dissipation of scalar variance, the cospectrum Φ_{CT} becomes (de Szoeke 1998)

$$\Phi_{CT} = [\Phi_C]^{1/2}[\Phi_T]^{1/2}. \tag{A4}$$

First, for a given data segment, we constructed Φ_S by combining corrected-Φ_C and corrected-Φ_T, and then the averaged Φ_S was constructed by averaging nearly 40 model spectra (the solid line shown in Fig. 13e). Here, we estimated α_1 and α_2 directly from the standard UNESCO formulations (Fofonoff and Millard 1983); for our sampling range, $29.1 < T < 29.4$°C and $33.9 < S < 34.2$ psu (Figs. 6b,c); the averaged values of α_1 and α_2 were 0.71 psu °C^{-1} and 6.83 psu (siemens m^{-1})$^{-1}$, respectively.

REFERENCES

Anderson, S. P., R. A. Weller, and R. Lukas, 1996: Surface boundary forcing and the mixed layer of the western Pacific warm pool: Observations and 1D model results. *J. Climate,* **9,** 3056–3085.

——, ——, and A. J. Plueddemann, 1998: Surface mixed layer response to freshwater flux: Observations and model results (abstract). *Eos, Trans. Amer. Geophys. Union,* **79** (1), Ocean Sci. Meet. Suppl., OS37.

Barenblatt, G. I., and G. I. Shapiro, 1984: A contribution to the theory of the wave fronts in dispersive dissipative media. *Izu. Akad. Sci. Nauk USSR, Atmos. Oceanic Phys.,* **20,** 277–284.

Brainerd, K. E., and M. C. Gregg, 1997: Turbulence and stratification on the TOGA-COARE microstructure-pilot cruise. *J. Geophys. Res.,* **102,** 10 437–10 455.

Businger, J. A., J. C. Wyngaard, Y. Izumi, and E. F. Bradley, 1971: Flux-profile relationships in the atmospheric surface layer. *J. Atmos. Sci.,* **28,** 181–189.

de Szoeke, R. A., 1998: The dissipation of fluctuating tracer variances. *J. Phys. Oceanogr.,* **28,** 2064–2074.

Donguy, J. R., 1987: Recent advances in the knowledge of the climatic variations in the tropical Pacific Ocean. *Progress in Oceanography,* Vol. 19, Pergamon 49–85.

Fairall, C. W., E. F. Bradley, D. P. Rogers, J. B. Edson, and G. S. Young, 1996: Bulk parameterization of air–sea fluxes for tropical ocean global atmosphere coupled ocean atmosphere response experiment. *J. Geophys. Res.,* **101,** 3747–3764.

Feng, M., P. Hacker, and R. Lukas, 1998: Upper ocean heat and salt balances in response to a westerly wind burst in the western equatorial Pacific during TOGA COARE. *J. Geophys. Res.,* **103,** 10 289–10 311.

Fofonoff, N. P., and R. C. Millard Jr., 1983: Algorithms for computation of fundamental properties of seawater. UNESCO Tech. Papers in Marine Science, UNESCO, Paris, France, 53 pp.

Gosenell, R., C. W. Fairall, and P. J. Webster, 1995: The sensible heat of rainfall in the tropical ocean. *J. Geophys. Res.,* **100,** 18 437–18 442.

Gregg, M. C., and W. Hess, 1985: Dynamics response calibration of Sea-Bird temperature and conductivity sensors. *J. Atmos. Oceanic Technol.,* **2,** 304–313.

——, C. S. Cox, and P. W. Hacker, 1973: Vertical microstructure measurements in the central North Pacific. *J. Phys. Oceanogr.,* **3,** 458–469.

——, T. Meagher, A. Pederson, and E. Aagaard, 1978: Low noise temperature microstructure measurements with thermistors. *Deep-Sea Res.,* **25,** 843–856.

Huyer, A., P. M. Kosro, R. Lukas, and P. Hacker, 1997: Upper-ocean thermohaline fields near 2°S, 156°E during TOGA-COARE, November 1992 to February 1993. *J. Geophys. Res.,* **102,** 12 749–12 784.

Keen, R. A., 1982: The cross-equatorial tropical cyclone pairs in the Southern Oscillation. *Mon. Wea. Rev.,* **110,** 1405–1416.

Kuroda, Y., and M. J. McPhaden, 1993: Variability in the western equatorial Pacific Ocean during Japanese Pacific climate study cruises in 1989 and 1990. *J. Geophys. Res.,* **98,** 4747–4759.

Levitus, S., 1982: *Climatological Atlas of the World Ocean.* NOAA Prof. Paper No. 13, U.S. Govt. Printing Office, 173 pp.

Lueck, R. G., and J. J. Picklo, 1990: Thermal inertia of conductivity cells: Observations with a Sea-Bird cell. *J. Atmos. Oceanic Technol.,* **7,** 756–768.

——, O. Hertzman, and T. R. Osborn, 1977: The spectral response of thermistors. *Deep-Sea Res.,* **24,** 951–970.

Lukas, R., and E. Lindstrom, 1991: The mixed layer of the western equatorial Pacific Ocean. *J. Geophys. Res.,* **96,** 343–357.

McPhaden, M. J., and S. P. Hayes, 1991: On the variability of winds, sea surface temperature, and surface layer heat content in the western equatorial Pacific. *J. Geophys. Res.,* **96,** 3331–3342.

——, H. P. Freitag, S. P. Hayes, B. A. Taft, Z. Chen, and K. Wyrtki, 1988: The response of the equatorial Pacific to a westerly wind burst in May 1986. *J. Geophys. Res.,* **93,** 10 589–10 603.

Monin, A. S., and A. M. Yaglom, 1975: *Statistical Fluid Mechanics: Mechanics of Turbulence.* Vol 2. The MIT Press, 874 pp.

Morison, J., R. Anderson, N. Larson, E. D'Asaro, and T. Boyd, 1994: The correction for thermal-lag effects in Sea-Bird CTD data. *J. Atmos. Oceanic Technol.,* **11,** 1151–1164.

Moum, J. N., and D. R. Caldwell, 1994: Experiment explores the

dynamics of ocean mixing. *Eos, Trans. Amer. Geophys. Union,* **75,** 489–504.

——, ——, and C. A. Paulson, 1989: Mixing in the equatorial surface layer. *J. Geophys. Res.,* **94,** 2005–2021.

O'Malley, R., P. M. Kosro, R. Lukas, and A. Huyer, 1993: Seasoar observations during COARE surveys cruise, W9211B, 12 December 1992 to 16 January 1993. College of Oceanic and Atmospheric Sciences, Oregon State University, Data Rep. 156, 426 pp. [Available from College of Oceanic and Atmospheric Sciences, Oregon State University, OC Admin. 104, Corvallis, OR 97331.]

Osborn, T. R., 1980: Estimates of the local rate of vertical diffusion from dissipation measurements. *J. Phys. Oceanogr.,* **10,** 83–89.

——, and C. S. Cox, 1972: Oceanic microstructure. *Geophys. Fluid Dyn.,* **3,** 321–345.

Paulson, C. A., and G. Lagerloef, 1993: Fresh surface lenses caused by heavy rain over the western equatorial Pacific Warm Pool during TOGA COARE (abstract). *Eos, Trans. Amer. Geophys. Union,* **74**(43), Fall Meet. Suppl., 125.

——, E. Leavitt, and R. G. Fleagle, 1972: Air–sea transfer of momentum, heat and water determined from profile measurements during BOMEX. *J. Phys. Oceanogr.,* **2,** 487–497.

Peters, H., M. C. Gregg, and J. M. Toole, 1988: On the parameterization of equatorial turbulence. *J. Geophys. Res.,* **93,** 1199–1281.

Philander, S. G. H., 1990: *El Niño, La Niña, and the Southern Oscillation,* Academic Press, 293 pp.

Price, J. F., R. A. Weller, and R. Pinkel, 1986: Diurnal cycling: Observations and models of the upper ocean response to diurnal heating, cooling, and wind mixing. *J. Geophys. Res.,* **91,** 8411–8427.

Samelson, R. M., and C. A. Paulson, 1988: Towed thermistor chain observations of fronts in the subtropical North Pacific. *J. Geophys. Res.,* **93,** 2237–2246.

Short, D. A., P. A. Kucera, B. S. Ferrier, J. C. Gerlach, S. A. Rutledge, and O. W. Thiele, 1997: Shipboard radar rainfall patterns within the TOGA COARE IFA. *Bull. Amer. Meteor. Soc.,* **78,** 2817–2836.

Smyth, W. D., D. Hebert, and J. N. Moum, 1996a: Local ocean response to a multiphase westerly wind burst. Part 1: The dynamic response. *J. Geophys. Res.,* **101,** 22 495–22 512.

——, ——, and ——, 1996b: Local ocean response to a multiphase westerly wind burst. Part 2: Thermal and freshwater response. *J. Geophys. Res.,* **101,** 22 513–22 533.

——, P. O. Zavialov, and J. N. Moum, 1997: Decay of turbulence in the upper ocean following sudden isolation from surface forcing. *J. Phys. Oceanogr,* **27,** 820–822.

Soloviev, A., and R. Lukas, 1997: Sharp frontal interfaces in near-surface layer of the ocean in the western equatorial Pacific Warm Pool. *J. Phys. Oceanogr.,* **27,** 999–1017.

——, ——, S. Asghar, and D. Khlebnikov, 1993: Coherent structures near the air–sea interface in the western Pacific Warm Pool (abstract). *Eos Trans. Amer. Geophys. Union,* **74** (43), Fall Meet. Suppl., p. 148.

Taylor, R., 1973: An atlas of Pacific rainfall. Rep. HIG-73-9, Hawaii Institute of Geophysics, University of Hawaii, Honolulu, 7 pp.

Tully, J. P., and F. G. Barber, 1960: An estuarine analogy in the sub-Arctic Pacific Ocean. *J. Fish. Res.,* **17,** 91–100.

Webster, P. J., and R. Lukas, 1992: TOGA COARE: The coupled ocean–atmosphere response experiment. *Bull. Amer. Meteor. Soc.,* **73** (9), 1377–1416.

Weller, R. A., and S. P. Anderson, 1996: Surface meteorology and air–sea fluxes in the western equatorial Pacific warm pool during the TOGA Coupled Ocean–Atmosphere Response Experiment. *J. Climate,* **9,** 1959–1990.

Wijesekera, H. W., and M. C. Gregg, 1996: Surface layer response to weak winds, westerly bursts, and rain squalls in the western Pacific Warm Pool. *J. Geophys. Res.,* **101,** 977–997.

Williams, R. M., and C. A. Paulson, 1977: Microscale temperature and velocity spectra in the atmospheric boundary layer. *J. Fluid Mech.,* **83,** 547–567.